

Upgrades to the Fluorescence Detectors of the Pierre Auger Observatory



THE UNIVERSITY
*of*ADELAIDE

Tristan William Sudholz

School of Physical Sciences
University of Adelaide

This dissertation is submitted for the degree of
Doctor of Philosophy

January, 2020

Declaration

I, Tristan William Sudholz, certify that this work contains no material which has been accepted for the award of any other degree or diploma in any university or other tertiary institution and, to the best of my knowledge and belief, contains no material previously published or written by another person, except where due reference has been made in the text. In addition, I certify that no part of this work will, in the future, be used in a submission for any other degree or diploma in any university or other tertiary institution without the prior approval of the University of Adelaide and where applicable, any partner institution responsible for the joint-award of this degree.

I give consent to this copy of my thesis, when deposited in the University Library, being made available for loan and photocopying, subject to the provisions of the Copyright Act 1968.

I also give permission for the digital version of my thesis to be made available on the web, via the University's digital research repository, the Library catalogue and also through web search engines, unless permission has been granted by the University to restrict access for a period of time.

Tristan William Sudholz

Abstract

Acknowledgements

Contents

Nomenclature	xi
Introduction	1
1 Cosmic-Rays	3
1.1 History of Cosmic-Rays	3
1.2 Energy Spectrum and Mass composition	3
1.3 Production Method and Sources	3
2 Detection of Cosmic-rays	7
2.1 Extensive Air Showers	7
2.2 Fluorescence Production	7
2.3 Atmospheric Effects	7
2.4 Detectors and History	7
3 Pierre Auger Observatory	9
3.1 Surface Detector	9
3.1.1 AugerPrime	9
3.2 Fluorescence Detector	9
3.2.1 Photomultiplier Tubes	12
3.3 Communication System and CDAS	12
3.4 Event Reconstruction	12
3.4.1 Surface Detector	12
3.4.2 Fluorescence Detector	12
3.5 Enhancements and future upgrades	12
4 EAS Selection Efficiency with Increased NSB	13
4.1 Selection Efficiency	14
4.2 Resolution and Bias	15
4.2.1 Comparing Simulated Data to Real Data	16
4.3 EAS Track Length in FD	16
5 Quantifying Characteristics of the FD PMT	23
6 Computer Simulation of FD PMT	29
7 Measuring FD PMT Gain Variance with CalA Data	35
7.1 Result of Pairs Method	35
7.2 Result of Averaging Sets of Traces Method	35
7.3 Result of Averaging Sets of Traces Method with Least Trimmed Squares	35

7.4 Result of Averaging Sets of Traces Method using Noise Distribution	35
8 Laboratory Simulation of FD shift	47
9 Evaluation of Cloud Camera Cuts	49
10 Conclusion	51
10.1 Future Work	51

Nomenclature

PAO	Pierre Auger Observatory
EAS	Extensive Air Shower
NSB	Night Sky Background
PE	Photo-electron
FD	Fluorescence Detector
SD	Surface Detector
PMT	Photomultiplier Tube
FLT	First Level Trigger

Introduction

- Define Cosmics Rays.
- The origins of the highest energy cosmic-rays still unknown.
- First detection by Pierre Auger in 1937 and the current detector looking at these energies is the Pierre Auger Observatory.
- Hybrid experiment containing both surface detectors and fluorescence detectors
- Surface detector has nearly 100% up-time while the fluorescence detectors only have 15% up-time.
- **** Proposal to extend the fluorescence detector up-time. To achieve this will have to operate while the moon is above the horizon. This will increase the level NSB and will have the PMTs run under a reduced gain to compensate. ****
- Photomultiplier Tubes are used as pixels within the camera of the fluorescence detectors and the aim of these thesis is to quantify the characteristics of the PMT under the reduced gain and increased.
- Outline a Summary of each chapter.

Cosmic-rays are particles that originate outside of the Earth atmosphere. These particles can be photons, hadronic or leptonic in nature [ref?]. In this thesis, when mentioning cosmic-rays I will mean the hadronic component unless specified otherwise. Cosmic-rays have been measured over a large range of energies (over 6 decades in energy) and it has many interesting features have been observed in this energy spectrum. One of the longest running mysteries is what happens at the highest energy. Since the first detection of extensive air showers by Pierre Auger in 1937 [ref], many different experiments have endeavoured to solve this mystery. The Pierre Auger Observatory [ref] is currently in operation to observe cosmic-rays at the highest energies.

The Pierre Auger Observatory is a hybrid experiment consisting of both surface detectors and fluorescence detectors. (Outline location) The surface detector has a nearly 100% operation up-time ref while the fluorescence detectors only 15% operation up-time [ref]. (Outline how PAO detects cosmic-rays, just need a brief summary).

A current proposal to extend the fluorescence detector operation up-time. Extended up-time would be beneficial as the fluorescence detectors image the entire extensive air shower and would increase the number of showers observed through out yearly observation. To achieve the extended operation the fluorescence detectors would have to be operated while the moon is above the horizon. While the moon is up, this would increase the Night Sky Background level and to compensate the Photomultiplier Tubes acting as the camera pixels would have to be run under reduced gain.

The aim of this thesis is to quantify the characteristics of the Photomultiplier Tubes operating under this reduced gain and outline any operation strategies. Outline of each chapter is as follows:

- Chapter 1: Cosmic-rays
Does this work as a new line
- Chapter 2: Detection of Cosmic-Rays
Add text here
- Chapter 3: The Pierre Auger Observatory
Add text here
- Chapter 4 : EAS Selection Efficiency with Increased NSB
Add text here
- Chapter 5 : Quantifying Characteristics of the FD PMT
Add text here
- Chapter 6 : Computer Simulation of the FD PMT
Add text here
- Chapter 7 : Measuring Gain Variance of the FD PMT with CalA data
Add text here
- Chapter 8 : Laboratory Simulation of FD Shifts
Add text here
- Chapter 9 : Effectiveness of Cloud Camera Cuts
Add text here
- Chapter 10: Conclusion
Future Work

Chapter 1

Cosmic-Rays

1.1 History of Cosmic-Rays

First detection of ionizing radiation.

1785: Coulomb found that electroscopes can spontaneously discharge by the action of the air and not by defective insulation

1835: Faraday confirms the observation by Coulomb, with better insulation technology

1879: Crookes measures that the speed of discharge of an electroscope decreased when pressure was reduced

1.2 Energy Spectrum and Mass composition

Cosmic-rays have been detected over a large range of energies from GeV (10^9 eV) to above EeV (10^{18} eV). Spectrum in Figure 1.1 shows the break at the knee and ankle and which type of experiments are most suited to measurement each part. Cosmic-ray spectrum starts out at E^{-2} and can be as steep as $E^{-2.7}$ at the highest energies.

Cosmic-rays can consist of protons to iron.

CR spectrum has many features. Main features are the knee, second knee and ankle. The knee is around 3×10^{15} .

Pierre Auger Observatory measurement of isotropy that shows that the cosmic-ray spectrum changes from predominately galactic to extra-galactic at the ankle.

Predicted Greisen-Zatsepin-Kuzmin (GZK) cut-off about 6×10^{19} . Cosmic-rays above this energy are theorised to interact with the cosmic microwave background radiation. Greisen independently of Kuz'man and Zatsepin all predicted this energy loss.

Pierre Auger Observatory measurement of X_{max} and the second moment $\sigma(X_{\text{max}})$ has mass composition information as well how this changes as a function of energy.

1.3 Production Method and Sources

- Bottom-Up Acceleration
 - Supernova explosions
 - AGN jets
 - other energetic processes

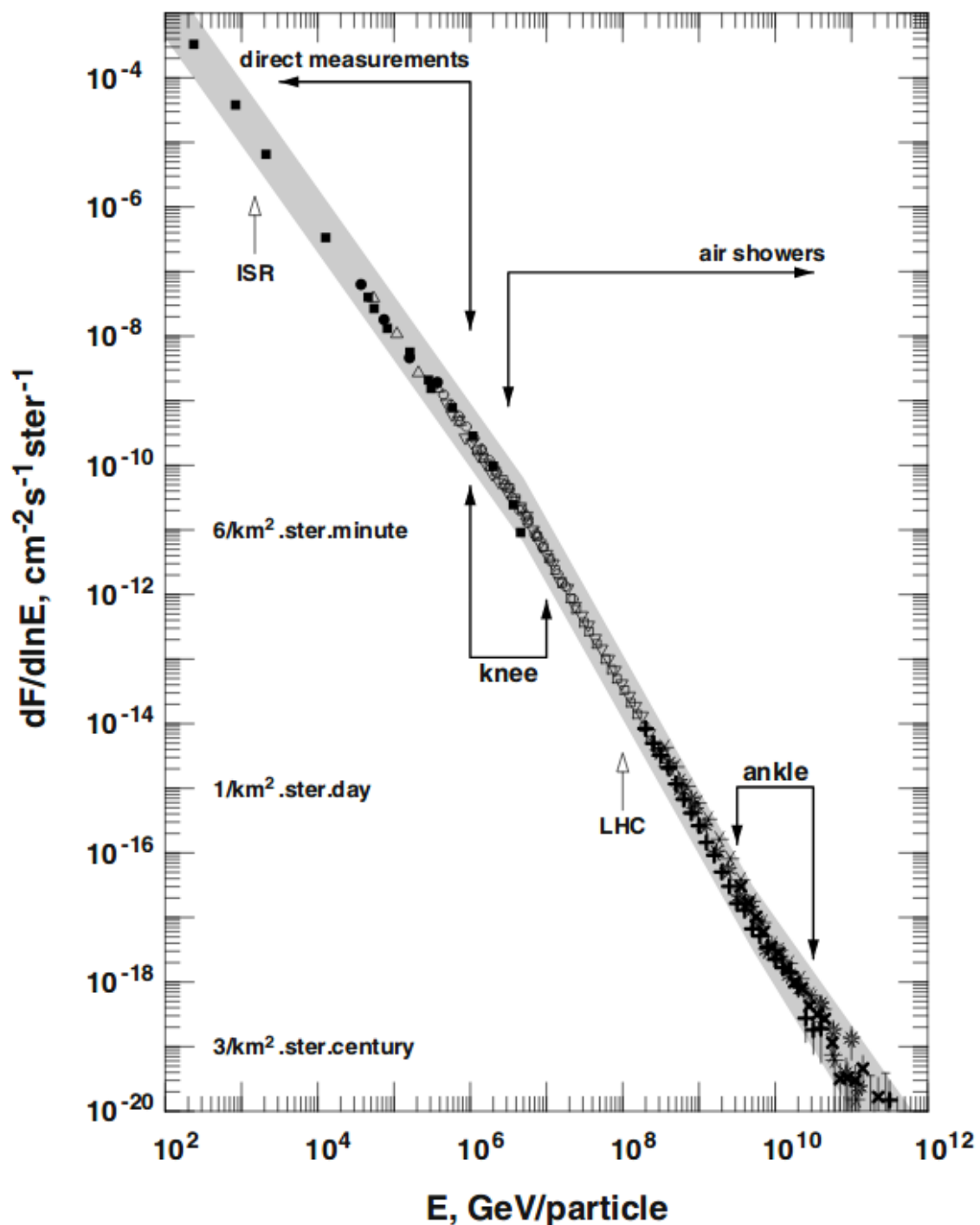


Figure 1.1: Measured energy spectrum of cosmic-rays from 100 GeV up to the highest detected energy.

dark matter annihilations.

- Top-Down Acceleration

Decay of massive relic particles

Typically associated with new physics beyond the standard model

Chapter 2

Detections of Cosmic-Rays

2.1 Extensive Air Showers

Use Earth's atmosphere as an interaction medium. Primary particle interacts with the molecules in the atmosphere to produce a cascade of secondary particles. This cascade of particles is referred to as an Extensive Air Shower (EAS). Hadronic primaries can produce pions, muons and other stuff. Mixture of a hadronic core with an electromagnetic component from the decay of π^0 .

Shower profile has particles produced until energy of individual secondary particles drop below the ionization threshold. Therefore the shower will reach a point of maximum particle number then will drop off.

2.2 Fluorescence Production

The charge particles of EAS interact with the nitrogen molecules in the atmosphere. This interaction turns the nitrogen molecule dipole like and when the nitrogen returns to a ground state, a photon is emitted. This emitted photon is termed fluorescence light. Fluorescence light is emitted isotropically and typically in the UV band (between 300 and 400 nm). *** Show wavelength profile ***

2.3 Atmospheric Effects

2.4 Detectors and History

Early Experiments:

Volcano Ranch

Haverah Park

SUGAR

Yakutsk array is located in Russia and has been operating in different forms since 1967. The array reached a maximum collecting area of 17 km^2 around 1990. Recently it has been reconfigured to have a collection area of 8 km^2 to study lower energy cosmic-rays.

Akeno Gaint Air Shower Array (AGASA) is located in Tokyo, Japan. Operating at an average altitude of 667 m above sea level from 1990 to 2004. The array consist of



Figure 2.1: Diagram of Cosmic-ray Extensive Air Showers.

over one hundred scintillator detectors covering 100 km^2 ***check this***. The timing measurements and data collection is achieved via interconnected optical fibers.

The Fly's Eye was the first successful air fluorescence detector operating from 1981 to 1993 at the Dugway Proving Grounds in Utah, USA. Fly's Eye achieved a time averaged aperture of about $100 \text{ km}^2 \text{sr}$ at the highest energies, considering it only operated on clear moonless nights.

HiRes improved on the Fly's Eye design by advancing resolution and sensitivity, This was achieved by increasing the telescope effective mirror area to 3.8 m^2 and reducing the camera pixel angular diameter to 1° .

Chapter 3

Pierre Auger Observatory

Science Goals of the Pierre Auger Observatory is to probe the origins and characteristics of cosmic rays above 10^{17} eV and to study the interactions of the most energetic particles observed in nature.

The Pierre Auger Observatory (PAO) is an hybrid detector that is located near Malargüe in the Mendoza Province, Argentina. PAO consists of 1660 Cherenkov water detector spread over 3000 km² by 24 fluorescence telescopes.

3.1 Surface Detector

The surface array consists of 1660 water Cherenkov tanks. The majority of tanks are configured with a spacing of 1500 metres while there is a small subset of tanks in front of the fluorescence telescopes at the Coihueco site with spacing of 750 metres.

The surface array has a duty cycle of nearly 100% and the maintenance cycle is so that no more then 20 tanks are down at any one time.

3.1.1 AugerPrime

3.2 Fluorescence Detector

There are four fluorescence detector site surrounding the surface array. At each fluorescence detector site there are six telescopes covering 180° in azimuth and 30° in elevation. At one site there are three extra telescopes with slightly greater then 90° in azimuth and cover 30° to 60° in elevation.

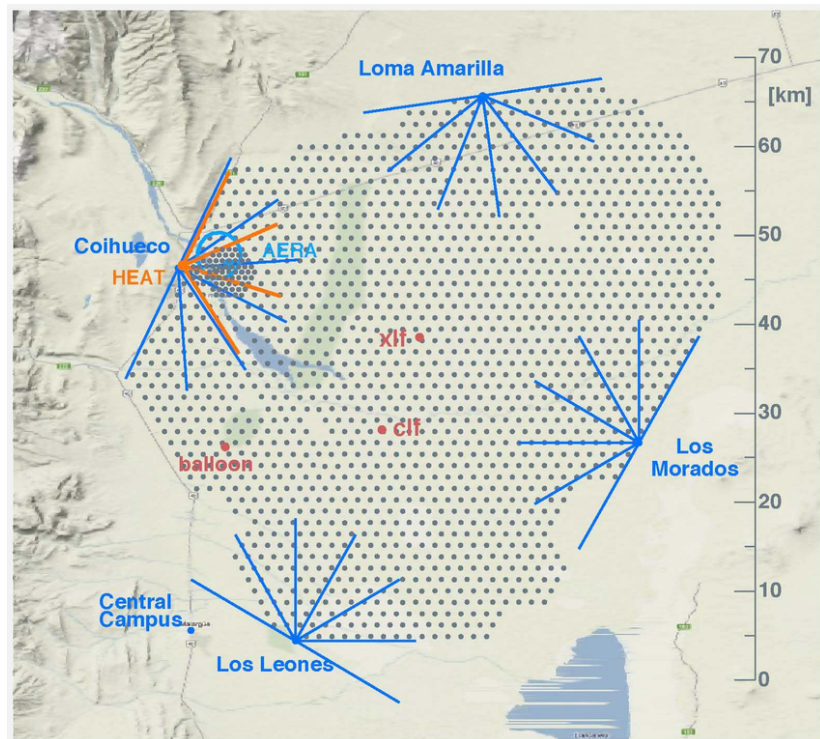


Figure 3.1: Image of layout of Pierre Auger Observatory located near Malargüe, Argentina.



Figure 3.2: Image of one of the fluorescence detector site (background) and one of the surface detectors (foreground).



Figure 3.3: Basic schematic of a surface detector.



Figure 3.4: Basic schematic of a fluorescence telescope.

3.2.1 Photomultiplier Tubes

3.3 Communication System and CDAS

3.4 Event Reconstruction

3.4.1 Surface Detector

3.4.2 Fluorescence Detector

3.5 Enhancements and future upgrades

Chapter 4

EAS Selection Efficiency with Increased NSB

Selection Efficiency of EAS under increased NSB

- Smearing real data with extra noise
- Simulating EAS with an increased NSB
- Talk about differences in smearing and simulating EAS (different triggering conditions)
- Energy and Xmas resolution and bias
- Rp bias
- differences in track length

Typically the NSB measured at PAO is in Units of ADC². As the signal is AC coupled, this is the variance around the zero and is directly proportional to the fluctuations in the NSB. The average value of the NSB is:

$$\sigma^2 \sim 25 \text{ ADC}^2 \quad (4.1)$$

Converting the variance into photons by using:

$$\sigma_{pe}^2 = [\sigma_{ADC}^2]^{sky} / A_G^2 \quad (4.2)$$

$$n_{ph} = \frac{\sigma_{pe}^2}{(1 + V_G)} \quad (4.3)$$

where σ_{pe} is the standard deviation of the photo-electron count, n_{ph} is the photon count and A_G is equal to:

$$A_G = \frac{1}{C_{FD}.f.Q} \quad (4.4)$$

where

A_G is the absolute gain (ADC/photo-electron)

C_{FD} is the FD pixel calibration constant.

Q is the Quantum efficiency of the PMT.

f is the efficiency of the telescope optics.

/*—— Find reference to number below ——*/

Assuming typical measured values for C_{FD} , Q and f shown in:

C_{FD}	4.5 photons/ADC
Q	0.29
f	0.465

Therefore can now calculate A_G from Eq. 4.4 and using

- Need graph of expected variance in ADC^2 for the moon above the horizon for different phases.
- Want to increase the duty cycle of FD by measuring EAS under moonlight. Most likely observe under quarter to half moon. This will increase the NSB upto a factor of 10.
- The aim of increasing the duty cycle of FD is to measure more EAS at the highest energy band ($> 10^{19.5}$ eV).
- Need more statistics at highest energy band to complement SD measurements.

4.1 Selection Efficiency

I investigated a couple of method evaluating increasing the NSB by different factors. The main increase of NSB will be from half moon which equates to an increase in NSB by a factor of 10. The two methods involved simulating increased NSB on measured data and with simulating. The measured data had increased noise introduced across the entire signal trace and I have labelled as the smearing method.

Selection Efficiency for the two methods are calculated via:

$$\text{Efficiency} = N_{\text{Selected}} / N_{\text{total}} \quad (4.5)$$

where for the Smearing method N_{total} is the total number of measured EAS events at standard NSB levels and N_{Selected} is the number of events after being reconstructed and passing the quality cuts with the increased NSB. For the simulations, N_{total} is the total number of simulated events before **need to check whether its the number of simulations before triggering or number of triggered events at standard NSB**.

Smearing method involves taking fluorescence telescope EAS data that have been reconstructed and passed all of the quality cuts and adding addition random variance in ADC^2 equivalent to an increased NSB from moonlight. The EAS data is then reconstructed and passed through the same quality cuts. This is a repartition of a similar method that M. Unger had performed in **2012**. **Also need to refer to the study done by Brue and Andrew Smith around 1999**. This was done so a deeper analysis could be performed to understand the underlying mechanics.

The simulations were done using the simulation modules for the FD's within the OffLine analysis programs. The EAS profiles were generated within CONEX and the original showers were generated through CORSIKA. The NSB was added to the EAS profiles before the FD are triggered. A hybrid trigger is used to involve the SD but the SD is simulated in a simple way just to get a simulated core position.

The smearing method was used as a proof of concept to show that EAS showers could still be reconstructed with the increased NSB. The limitation was that EAS were used that already triggered the FD's normally. The full simulation using CONEX showers was used to full test trigger conditions through to reconstruction. The simulations are not an 100% accurate representation of the POA array so that will introduce some differences too.

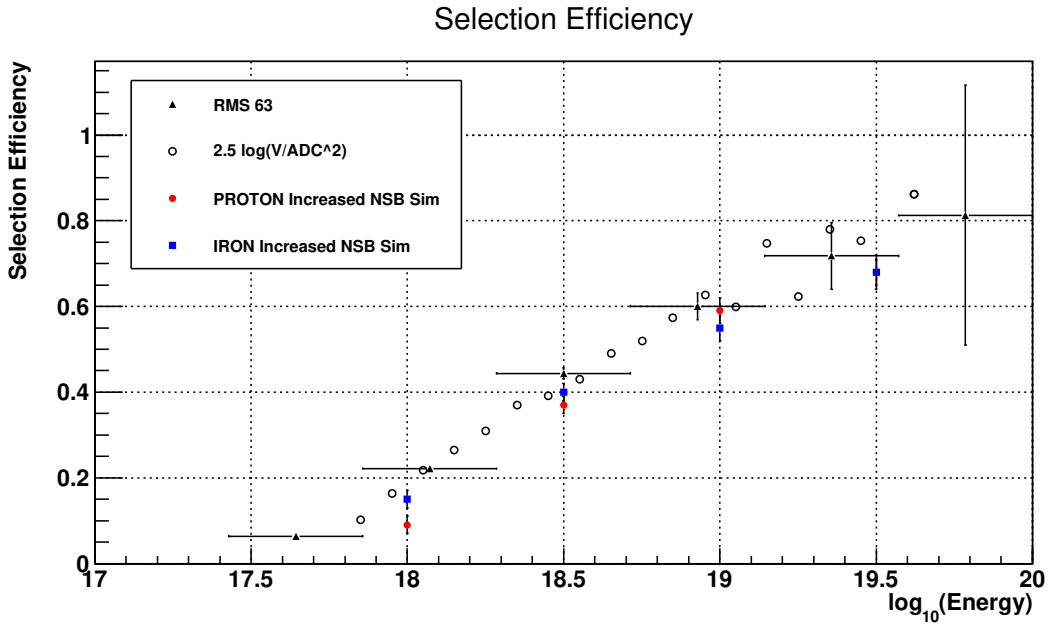


Figure 4.1: Selection Efficiency plot containing data from both the Smearing method and simulated showers. These results are compared to the work done by M. Unger.

4.2 Resolution and Bias

To further evaluate the effects of increasing the NSB on the quality of the reconstructed EAS data, I look at the resolution and bias of both the reconstructed energy and reconstructed Xmax. A quick reminder that Xmax is the measurement of the brightest part of the shower relating to the maximum number of particles produced. For the smearing method the energy and Xmax bias is comparing to the measured data taken at standard NSB levels to the reconstructed with the increased NSB levels. For the simulations the energy and Xmax bias can be calculated using the true energy and Xmax values used to generate each EAS profile.

The trend of the energy resolution for both methods is that as the energy of the EAS event increases the bias decreases. This was expected as the energy of the shower increases the brighter and longer the track that is observed. A brighter and longer track allows for a better reconstruction.

- Need to find out what's a good bias value for energy and Xmax.

the energy and Xamx bias is calcualted via:

$$\Delta E = \frac{E_{\text{recon}} - E_{\text{true}}}{E_{\text{true}}} \quad (4.6)$$

$$\Delta E = \frac{E_{\text{IncreasedNSB}} - E_{\text{StandardNSB}}}{E_{\text{StandardNSB}}} \quad (4.7)$$

$$\Delta X_{\text{max}} = X_{\text{max,recon}} - X_{\text{max,true}} \quad (4.8)$$

$$\Delta X_{\text{max}} = X_{\text{max,IncreasedNSB}} - X_{\text{max,StandardNSB}} \quad (4.9)$$

The energy and Xmax resolution is calculated via:

$$\sigma_{\text{res}} = \left(\frac{1}{N} \sum \frac{1}{\sigma_i^2} \right)^{1/2} \quad (4.10)$$

4.2.1 Comparing Simulated Data to Real Data

Think about where to locate this section.

Comparing the simulated data with real data. Checking to make sure that the simulation data is a good representation of reality. Looking at the Xmax distribution there is no need for a direction comparison as I only simulated proton and iron primaries and was not concern with have a particular mixtures. The other parameter I checked was the zenith angle distribution, distance to Xmax and distance to the shower axis (R_P). The simulated profiles have similar shapes when both histograms are normalised to area of 1. For zenith angle distribution I simulated the EAS events upto a zenith angle of 60°so that the reason for the cut-off in the simulated data.

4.3 EAS Track Length in the FD's

One other parameter that was investigate was the shower track length observed by the FD's. It was expected that as the NSB increased the average observed shower track length would decrease.

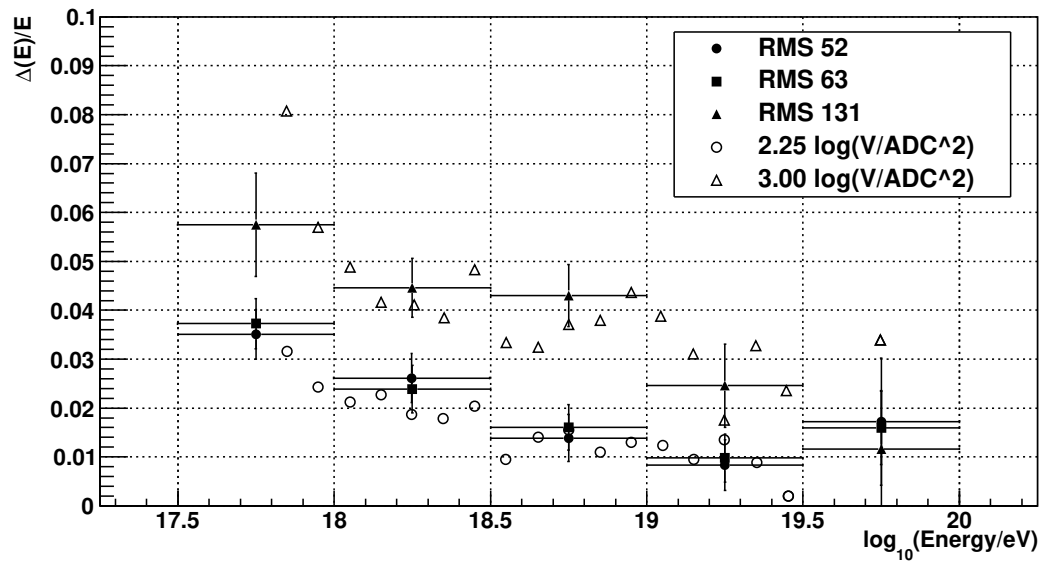


Figure 4.2: Energy Bias using Smearing Method.

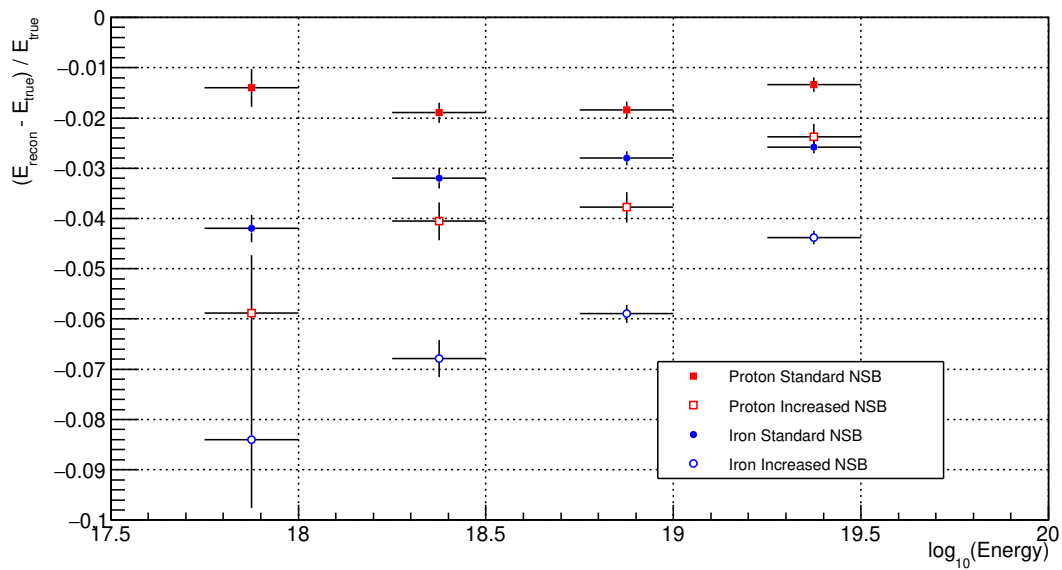


Figure 4.3: Energy Bias using simulated data.

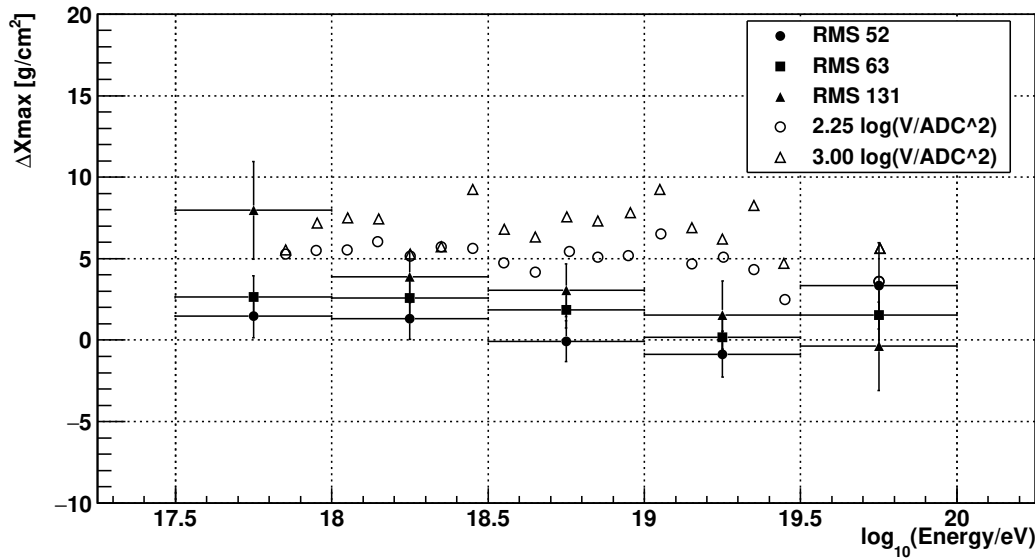


Figure 4.4: Xmax Bias using Smearing Method.

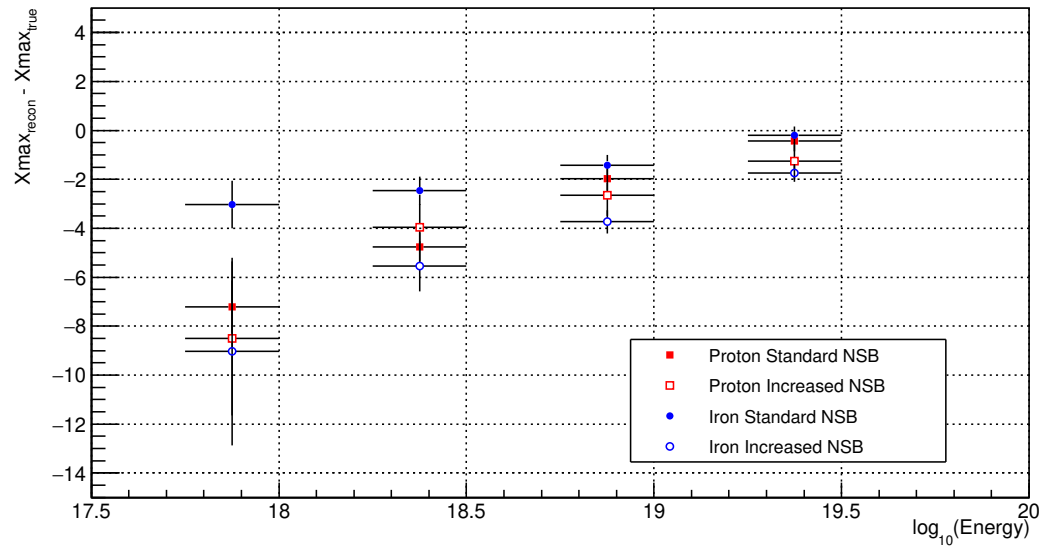


Figure 4.5: Xmax Bias using simulated data.

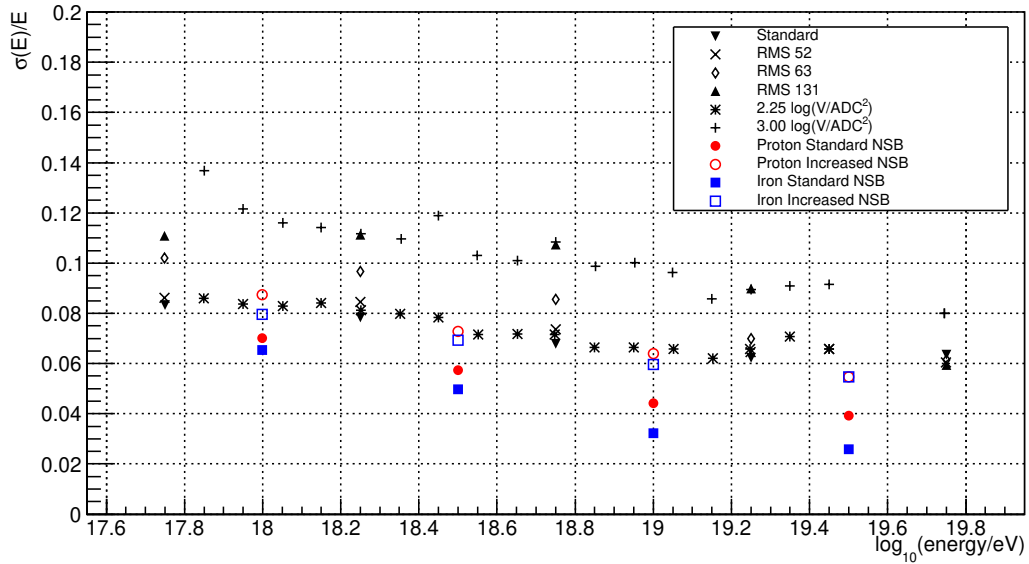


Figure 4.6: Energy Resolution using both Smearing Method data and simulated showers.

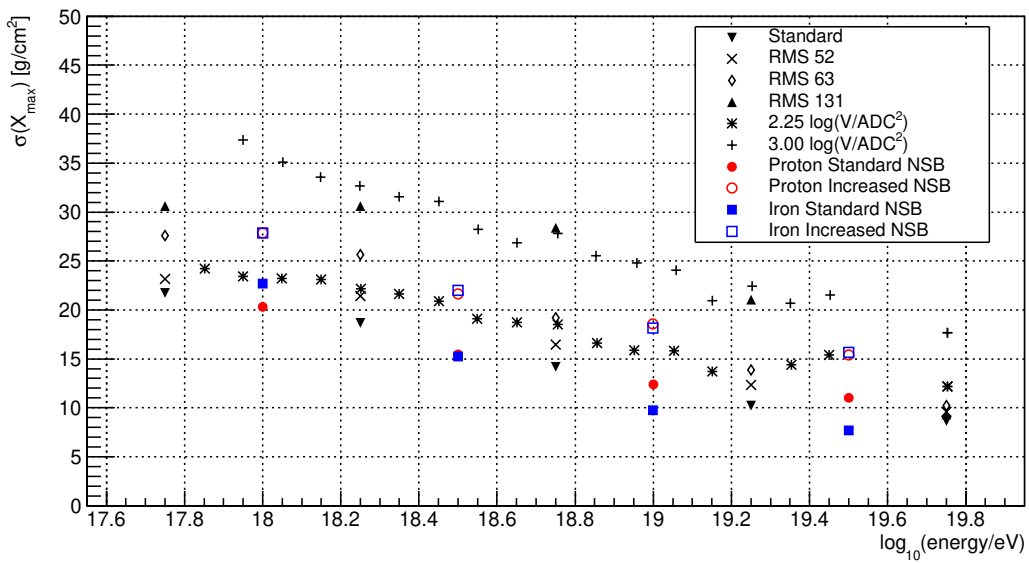


Figure 4.7: Xmax Resolution using both Smearing Method data and simulated showers.

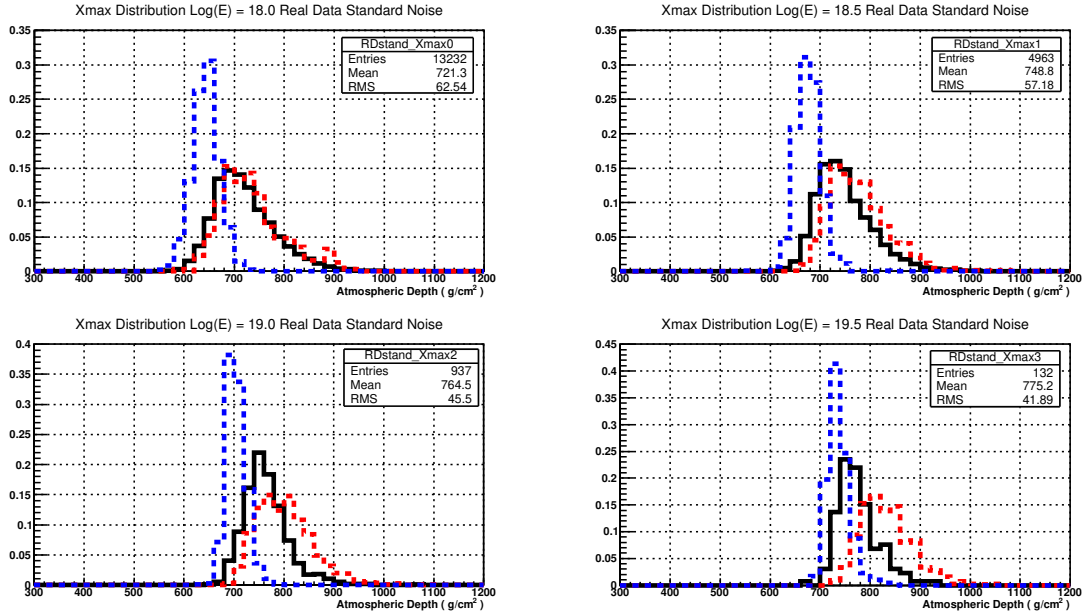


Figure 4.8: Distribution of Xmax with Real Data and simulation of proton and iron showers.

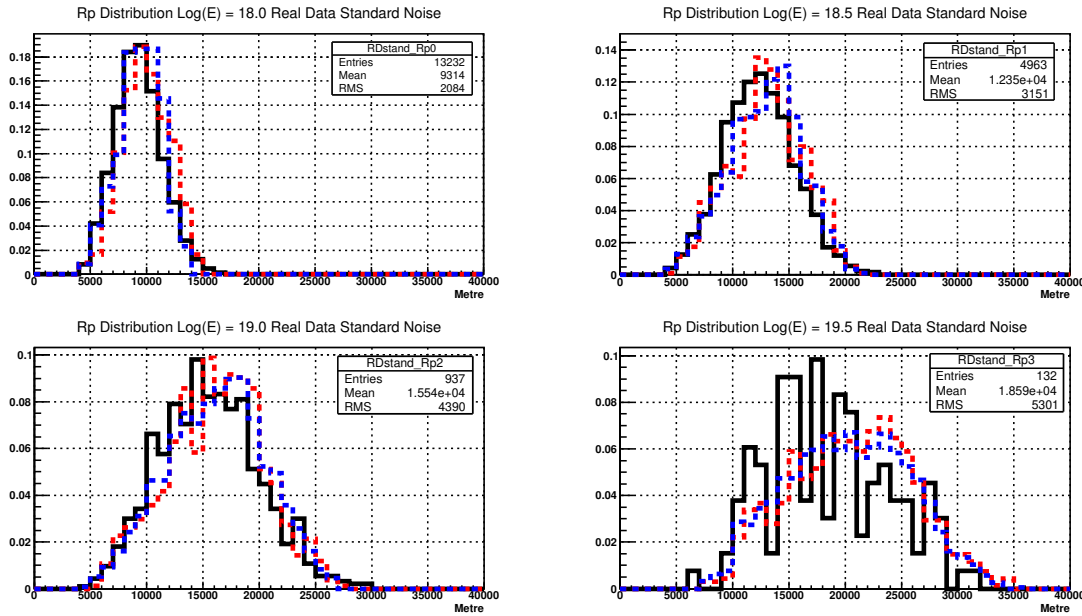


Figure 4.9: Distribution of Rp with Real Data and simulation of proton and iron showers.

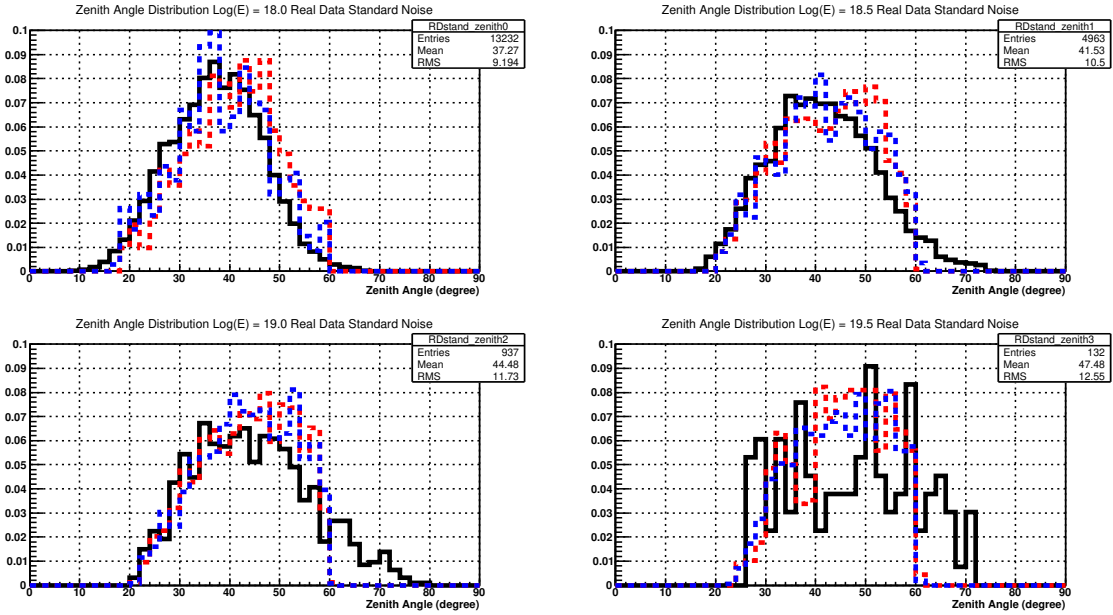


Figure 4.10: Distribution of Zenith angle with Real Data and simulation of proton and iron showers.

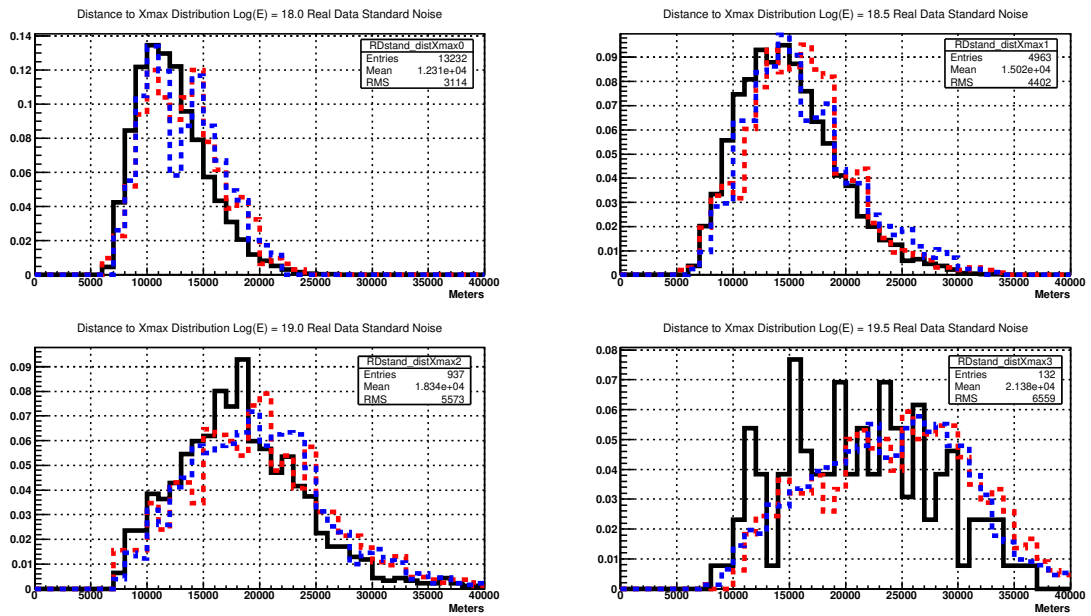


Figure 4.11: Distribution of Distance to Xmax with Real Data and simulation of proton and iron showers.

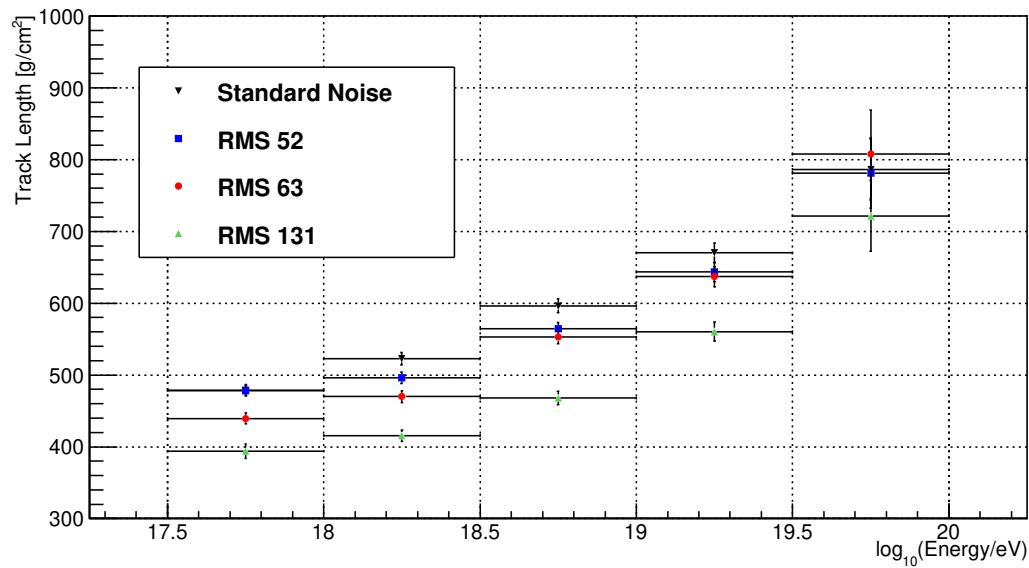


Figure 4.12: Track length using Smearing method.

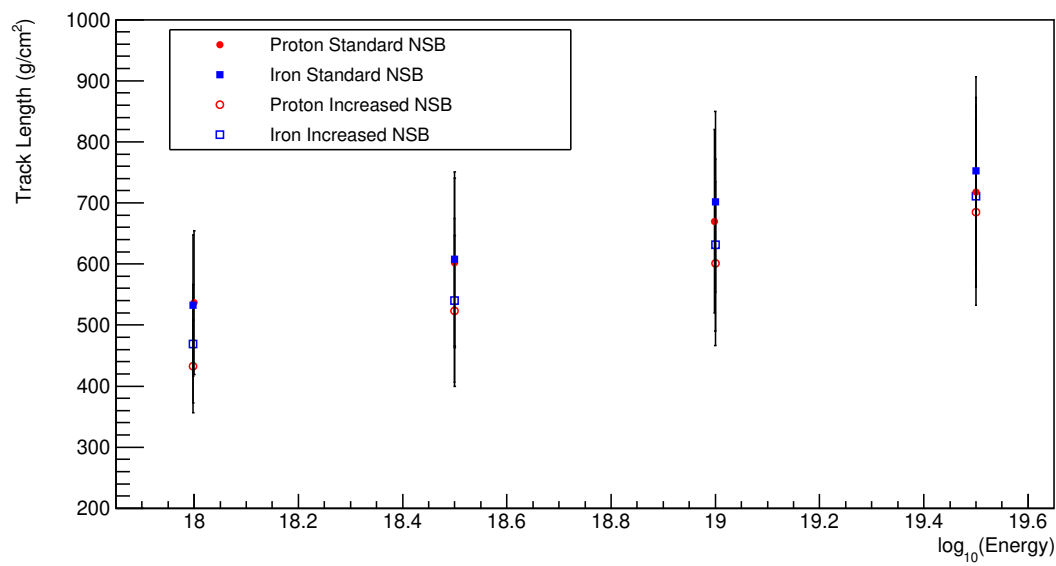


Figure 4.13: Track length using simulation of proton and iron CONEX showers.

Chapter 5

Quantifying Characteristics of the FD PMT

Characterising the PMT at 600V and 900V

- Using the characteristics of the PMT at 900V as a baseline
- Measure linearity
- ND filters vs Two LED method
- Pulse shape?
- temperature effects
- dark noise?

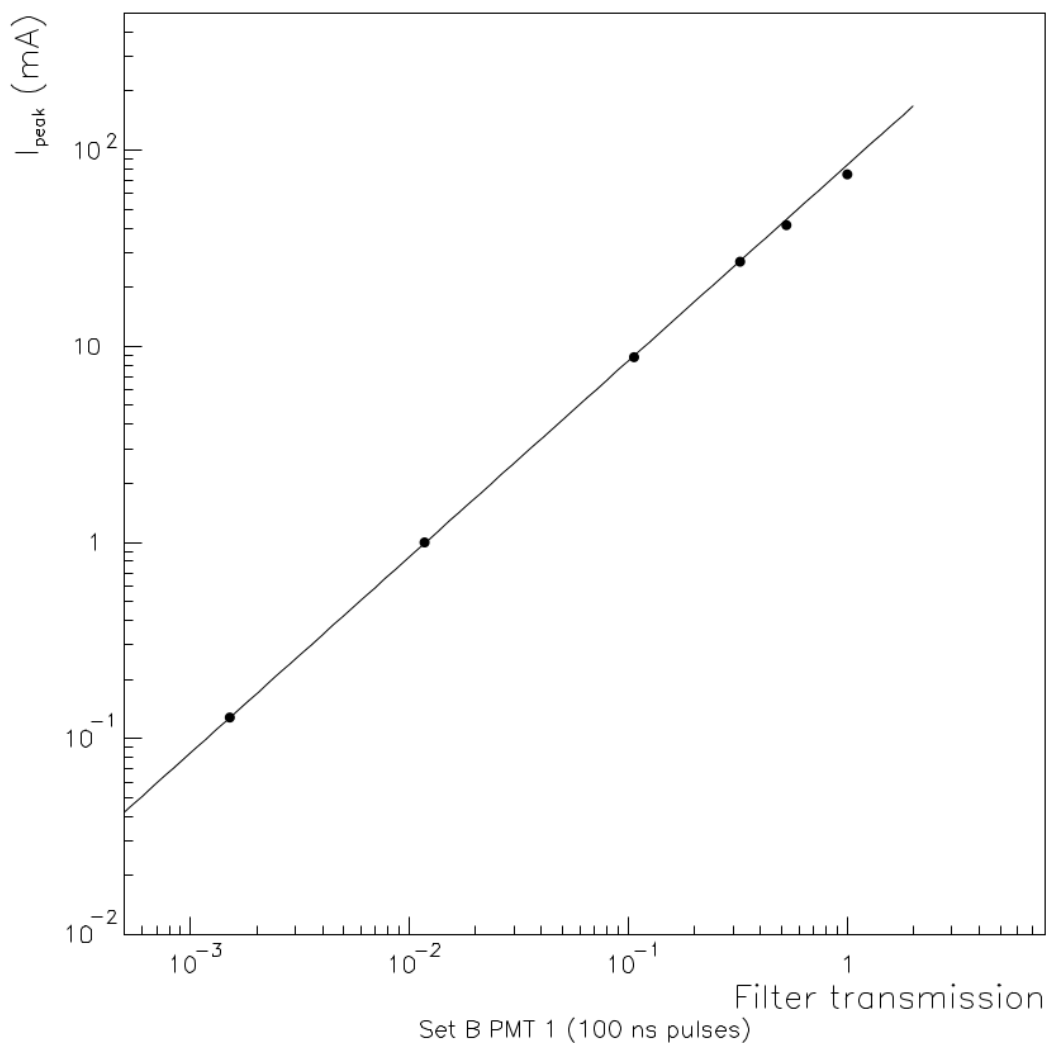
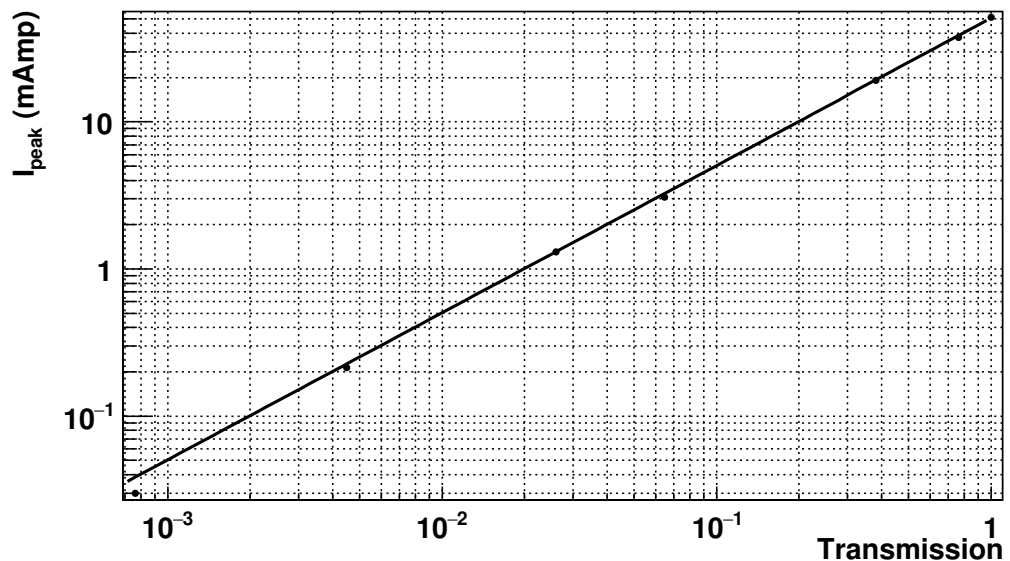
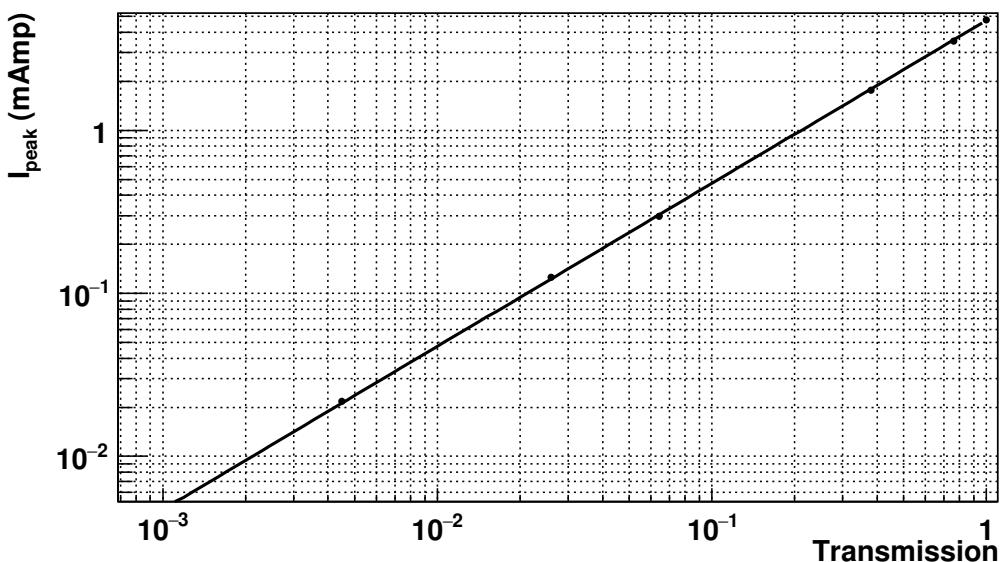


Figure 5.1: Previous PMT linearity test done by Privitera et. al. 1999 with Neutral density filters.

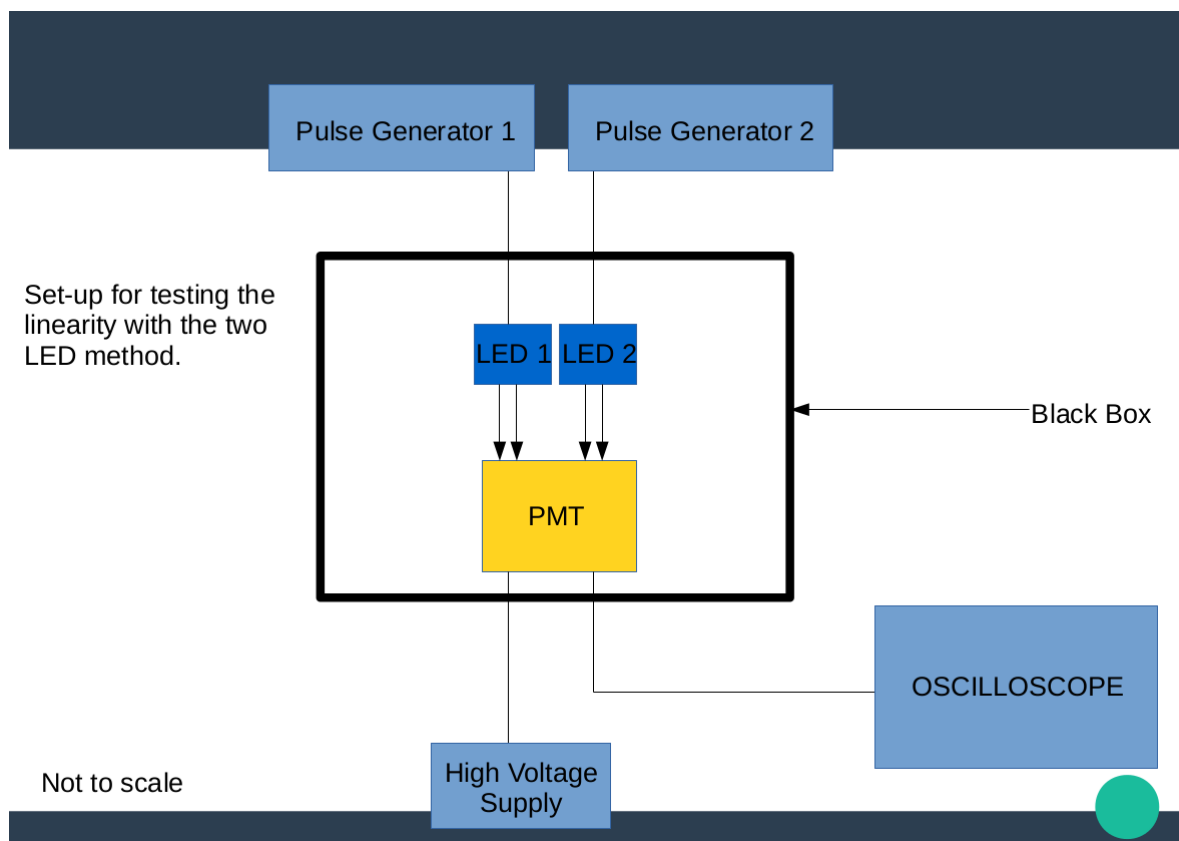


(a)



(b)

Figure 5.2: Neutral density method at 900V and 600V.



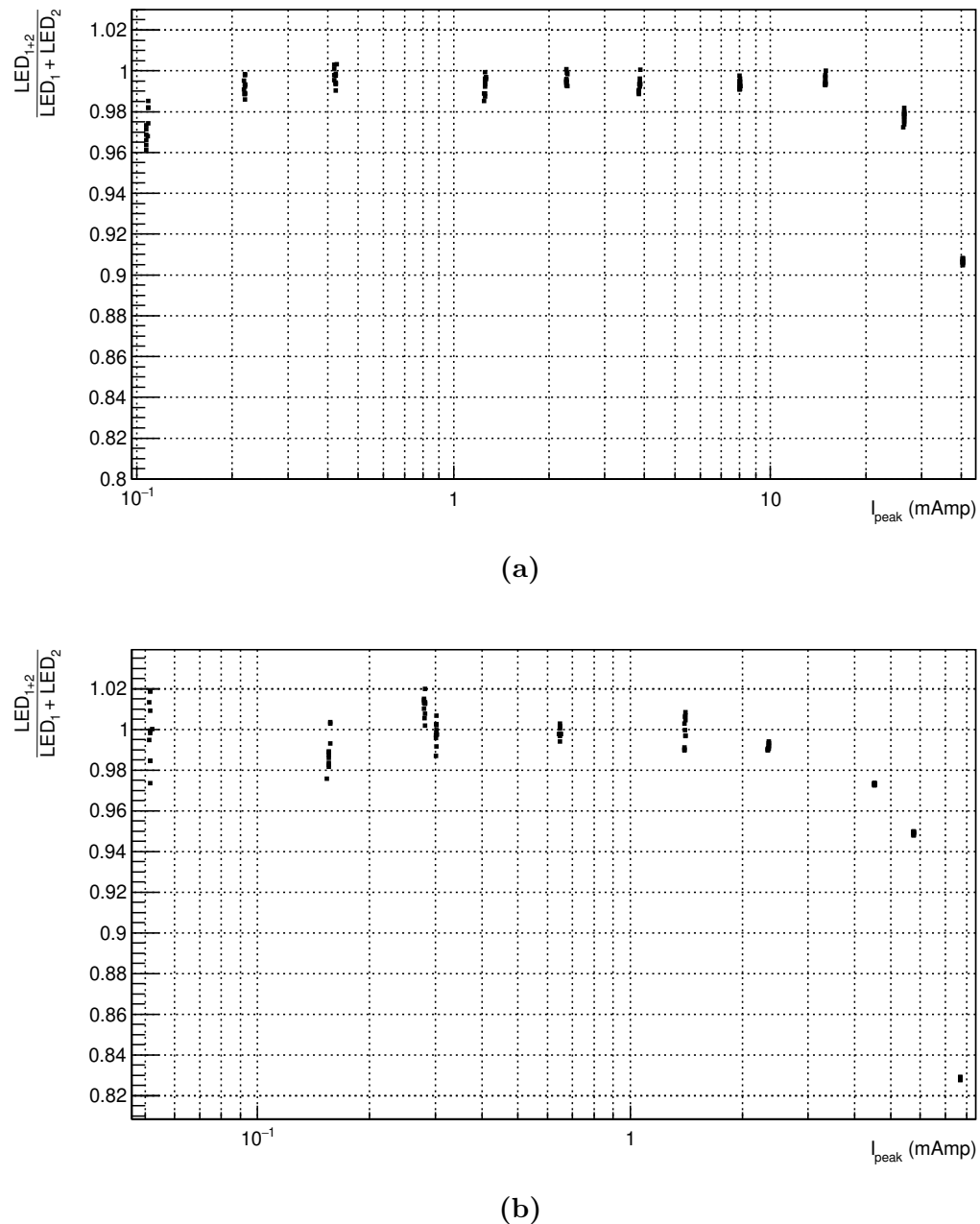


Figure 5.3: Two LED method at 900V and 600V.

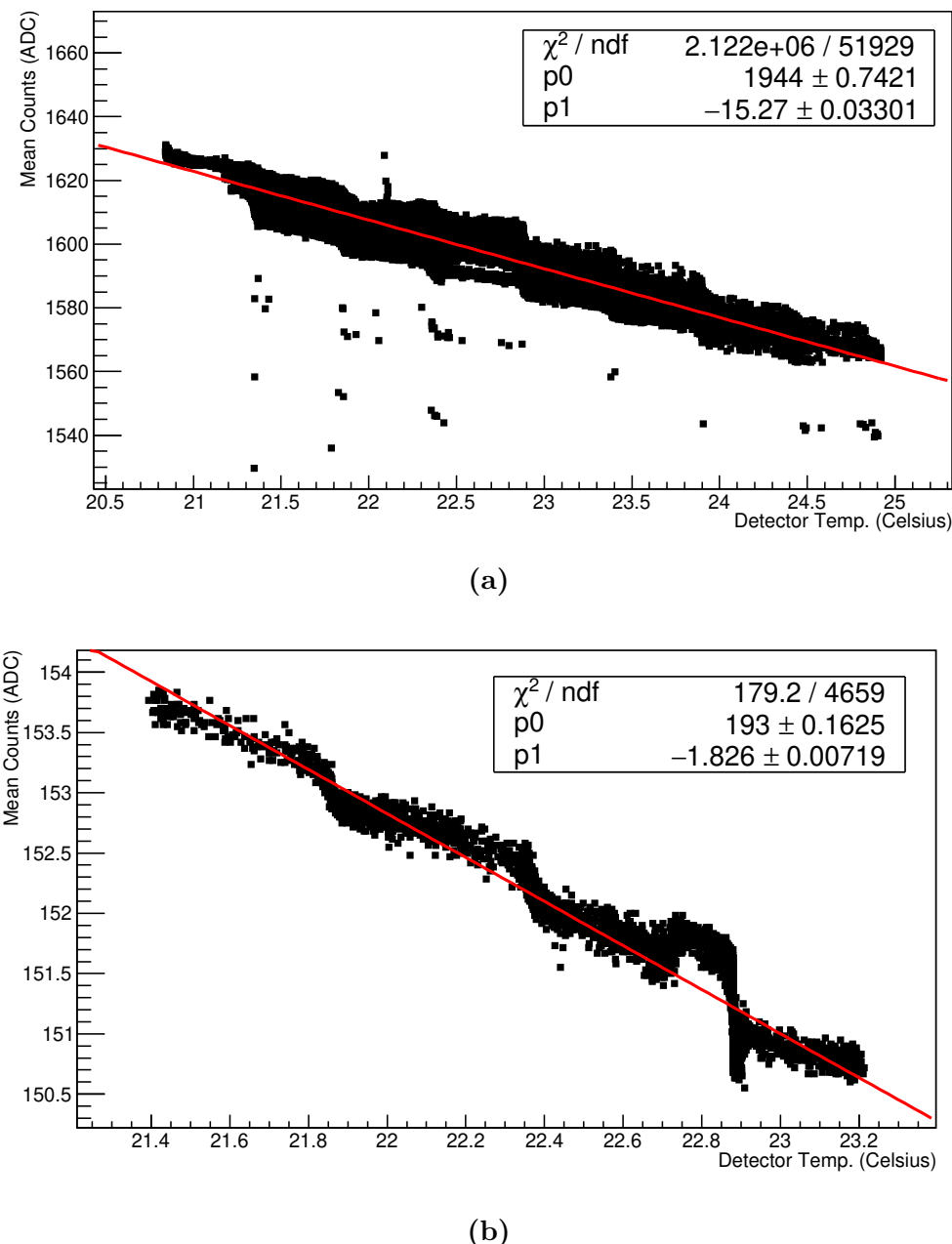


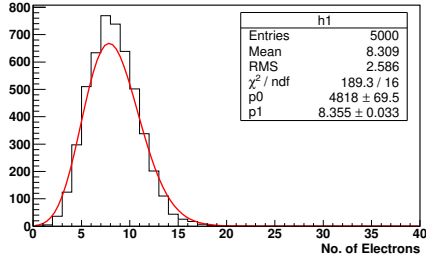
Figure 5.4: Showing the how PMT gain correlates with surrounding temperature.

Chapter 6

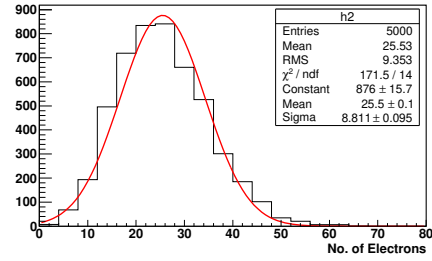
Computer Simulation of FD PMT

Simulating the FD PMT under differing NSB and for different reasons.

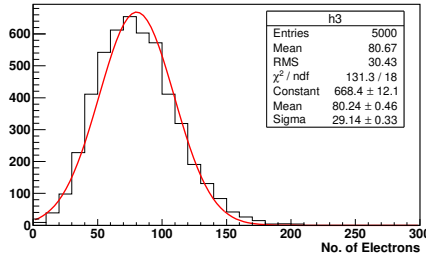
- Theoretical value for Gain Variance
- PMT Gain Variance
- Show both for flat distribution and Gaussian variations for dynodes
- Results
- FD FLT under increased NSB
- Kv simulation under increased NSB?



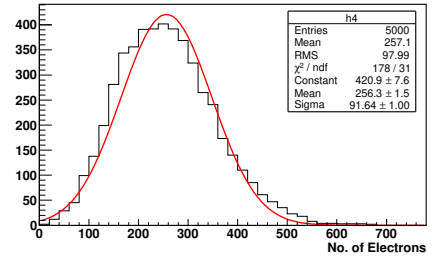
(a) Distribution of simulated electrons leaving dynode 1. The red line is a fitted Poisson distribution.



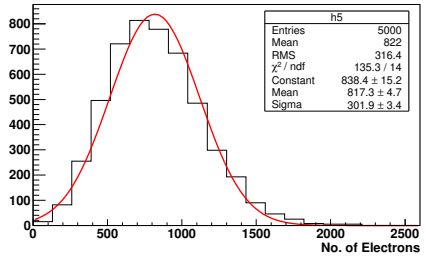
(b) Distribution of simulated electrons leaving dynode 2. The red line is a fitted Gaussian distribution.



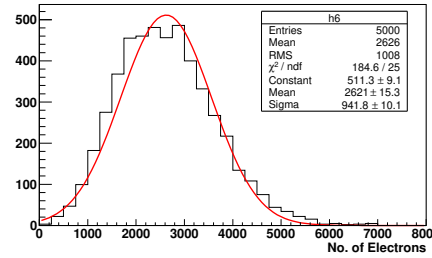
(c) Distribution of simulated electrons leaving dynode 3. The red line is a fitted Poisson distribution.



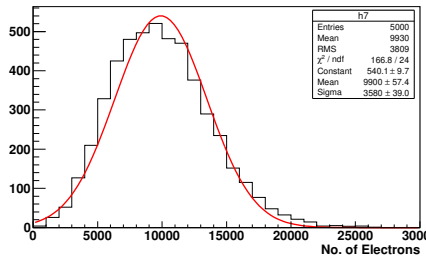
(d) Distribution of simulated electrons leaving dynode 4. The red line is a fitted Gaussian distribution.



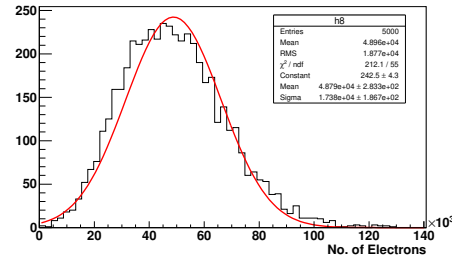
(e) Distribution of simulated electrons leaving dynode 5. The red line is a fitted Poisson distribution.



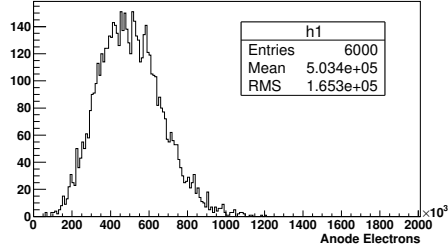
(f) Distribution of simulated electrons leaving dynode 6. The red line is a fitted Gaussian distribution.



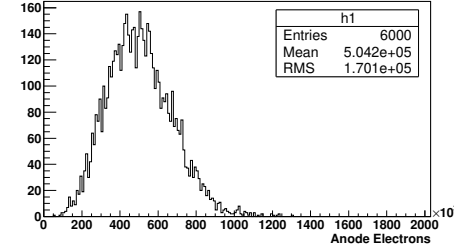
(g) Distribution of simulated electrons leaving dynode 7. The red line is a fitted Poisson distribution.



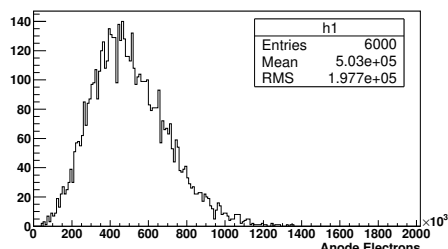
(h) Distribution of simulated electrons leaving dynode 8. The red line is a fitted Gaussian distribution.



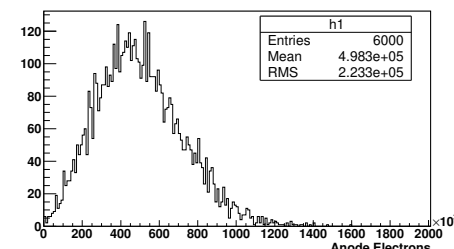
(a) Simulated observed signal from PMT anode with 8 stages and gain of 5×10^5 . Poisson fluctuations at each stage only. No each Gaussian broadening at any dynode.



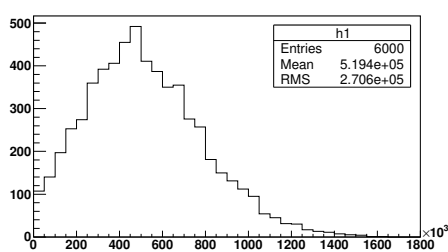
(b) Simulated observed signal from PMT anode with 8 stages and gain of 5×10^5 . Poisson fluctuations at each stage only. Added Gaussian broadening at each dynode of 10%.



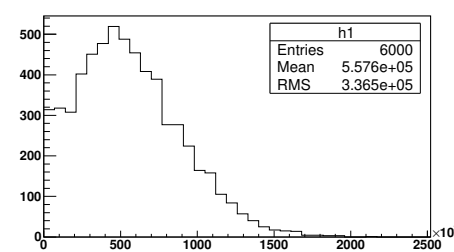
(c) Simulated observed signal from PMT anode with 8 stages and gain of 5×10^5 . Poisson fluctuations at each stage only. Added Gaussian broadening at each dynode of 20%.



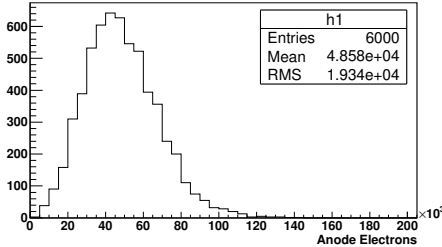
(d) Simulated observed signal from PMT anode with 8 stages and gain of 5×10^5 . Poisson fluctuations at each stage only. Added Gaussian broadening at each dynode of 30%.



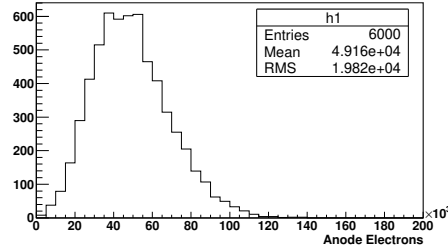
(e) Simulated observed signal from PMT anode with 8 stages and gain of 5×10^5 . Poisson fluctuations at each stage only. Added Gaussian broadening at each dynode of 40%.



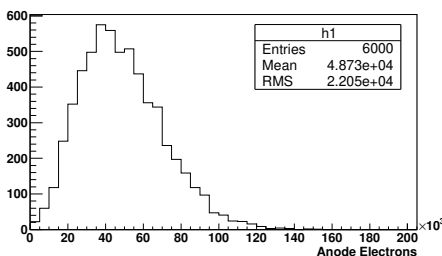
(f) Simulated observed signal from PMT anode with 8 stages and gain of 5×10^5 . Poisson fluctuations at each stage only. Added Gaussian broadening at each dynode of 50%.



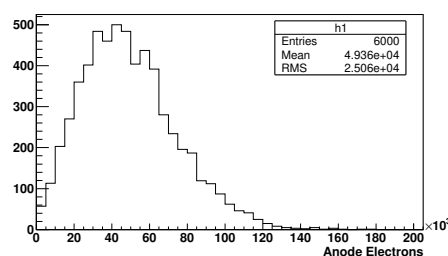
(a) Simulated observed signal from PMT anode with 8 stages and gain of 5×10^4 . Poisson fluctuations at each stage only. No each Gaussian broadening at any dynode.



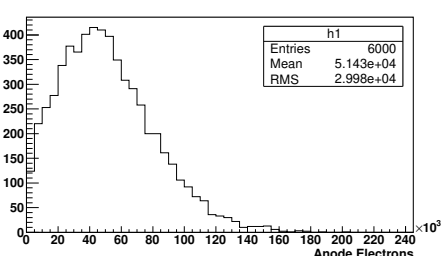
(b) Simulated observed signal from PMT anode with 8 stages and gain of 5×10^4 . Poisson fluctuations at each stage only. Added Gaussian broadening at each dynode of 10%.



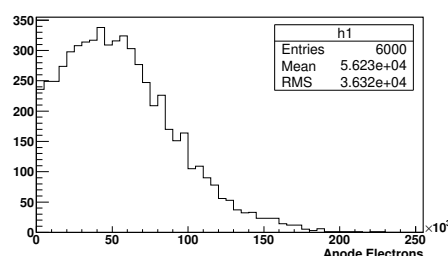
(c) Simulated observed signal from PMT anode with 8 stages and gain of 5×10^4 . Poisson fluctuations at each stage only. Added Gaussian broadening at each dynode of 20%.



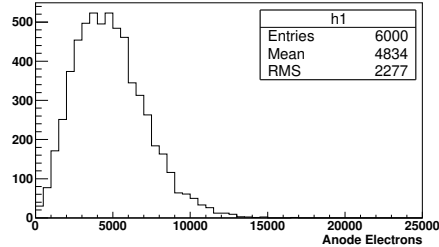
(d) Simulated observed signal from PMT anode with 8 stages and gain of 5×10^4 . Poisson fluctuations at each stage only. Added Gaussian broadening at each dynode of 30%.



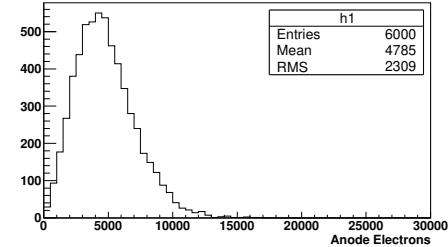
(e) Simulated observed signal from PMT anode with 8 stages and gain of 5×10^4 . Poisson fluctuations at each stage only. Added Gaussian broadening at each dynode of 40%.



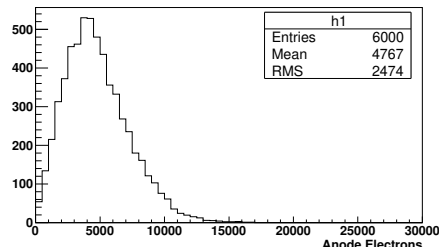
(f) Simulated observed signal from PMT anode with 8 stages and gain of 5×10^4 . Poisson fluctuations at each stage only. Added Gaussian broadening at each dynode of 50%.



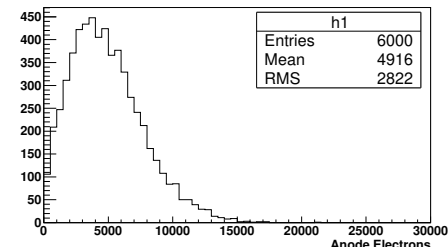
(a) Simulated observed signal from PMT anode with 8 stages and gain of 5×10^3 . Poisson fluctuations at each stage only. No each Gaussian broadening at any dynode.



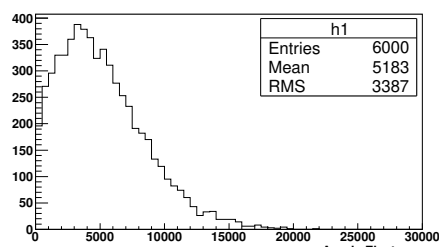
(b) Simulated observed signal from PMT anode with 8 stages and gain of 5×10^3 . Poisson fluctuations at each stage only. Added Gaussian broadening at each dynode of 10%.



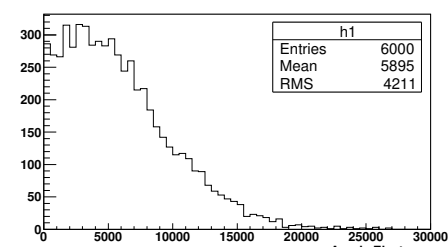
(c) Simulated observed signal from PMT anode with 8 stages and gain of 5×10^3 . Poisson fluctuations at each stage only. Added Gaussian broadening at each dynode of 20%.



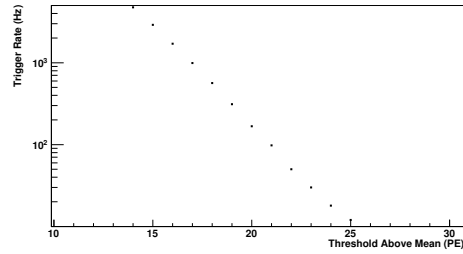
(d) Simulated observed signal from PMT anode with 8 stages and gain of 5×10^3 . Poisson fluctuations at each stage only. Added Gaussian broadening at each dynode of 30%.



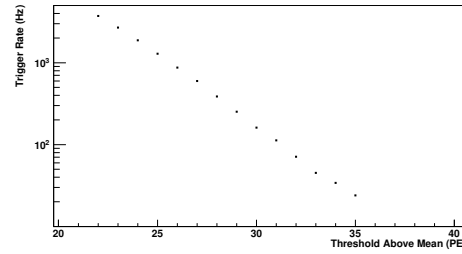
(e) Simulated observed signal from PMT anode with 8 stages and gain of 5×10^3 . Poisson fluctuations at each stage only. Added Gaussian broadening at each dynode of 40%.



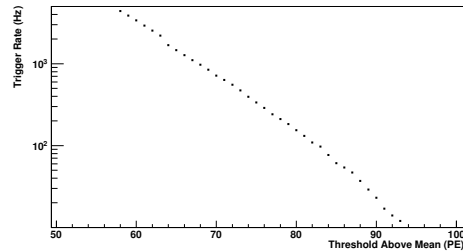
(f) Simulated observed signal from PMT anode with 8 stages and gain of 5×10^3 . Poisson fluctuations at each stage only. Added Gaussian broadening at each dynode of 50%.



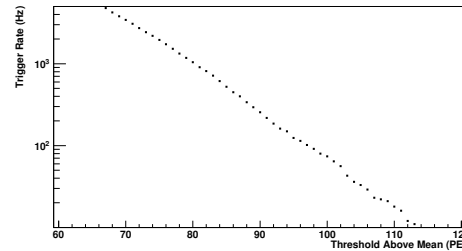
(a) FLT simulation with NSB of 2.71 pe / 100ns.



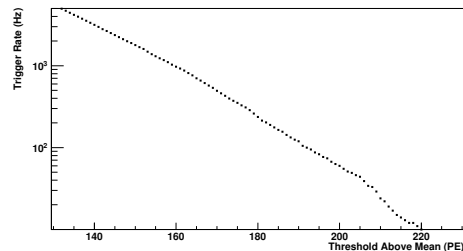
(b) FLT simulation with NSB of 6.60 pe / 100ns.



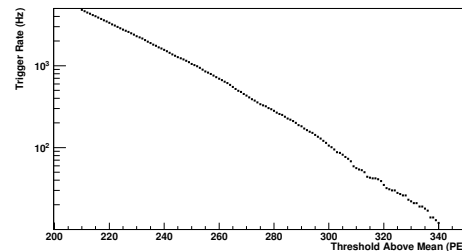
(c) FLT simulation with NSB of 46.8 pe / 100ns.



(d) FLT simulation with NSB of 65.8 pe / 100ns.



(e) FLT simulation with NSB of 263 pe / 100ns.



(f) FLT simulation with NSB of 657 pe / 100ns.

Chapter 7

Measuring FD PMT Gain Variance with CalA Data

Measuring Gain Variance of FD PMT with CalA Data

- Measuring Gain Variance in the lab did not work. Equipment was not sensitive enough to the low current.
- There were issues with calibrating the LED light source with another PMT (QE curve and wavelength response not the same?)
- Using Low/Standard measurements of CalA to find Gain Variance Ratio
- Two different methods
- Bootstrap method to find uncertainties on Method 2

7.1 Result of Pairs Method

7.2 Result of Averaging Sets of Traces Method

7.3 Result of Averaging Sets of Traces Method with Least Trimmed Squares

7.4 Result of Averaging Sets of Traces Method using Noise Distribution

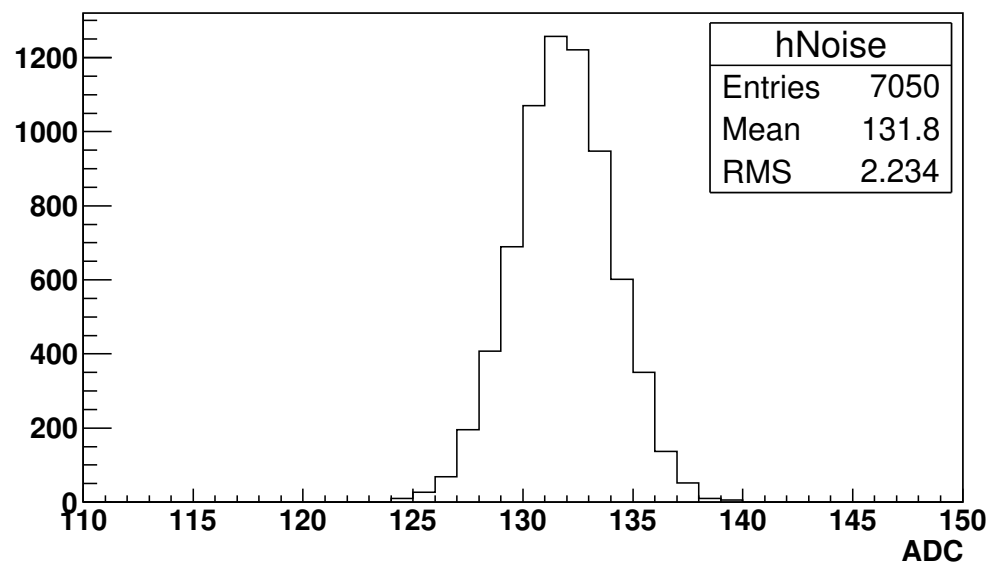


Figure 7.1

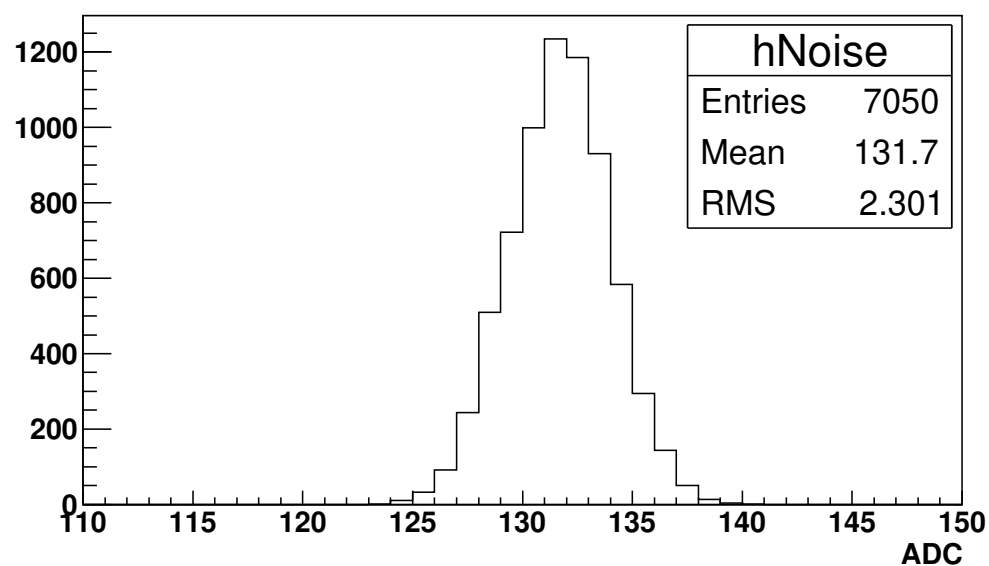


Figure 7.2

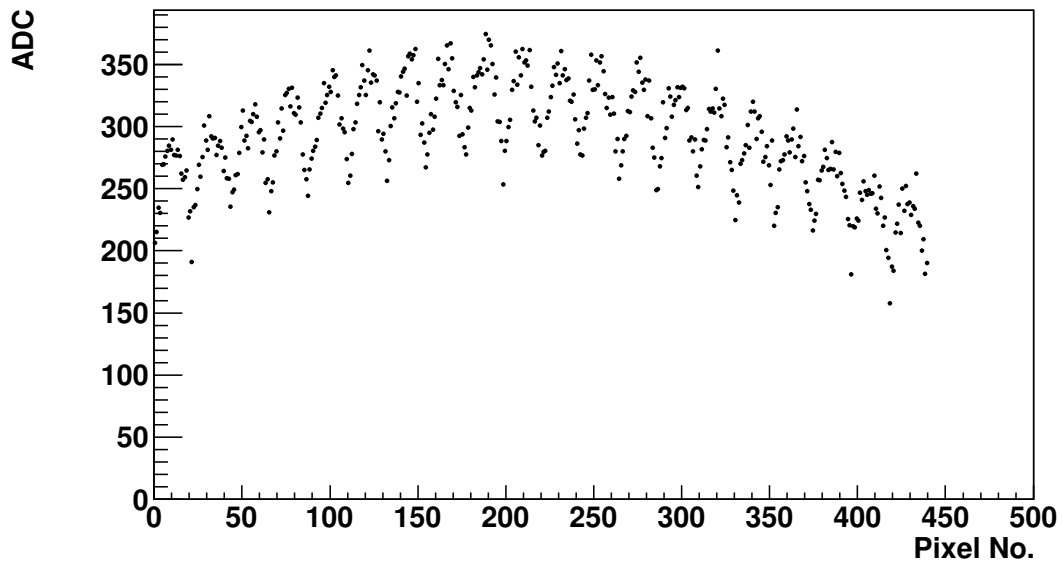


Figure 7.3

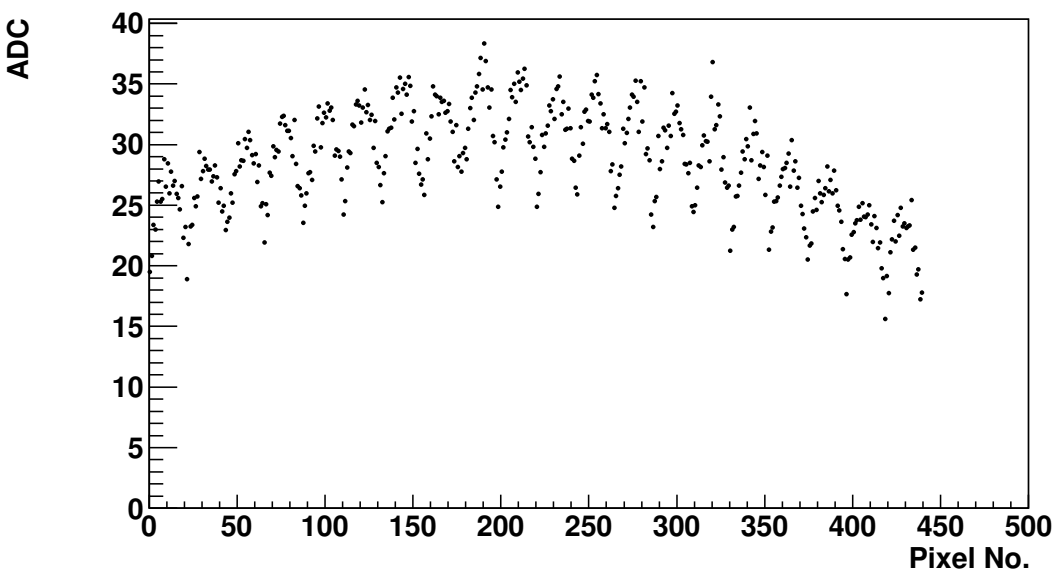


Figure 7.4

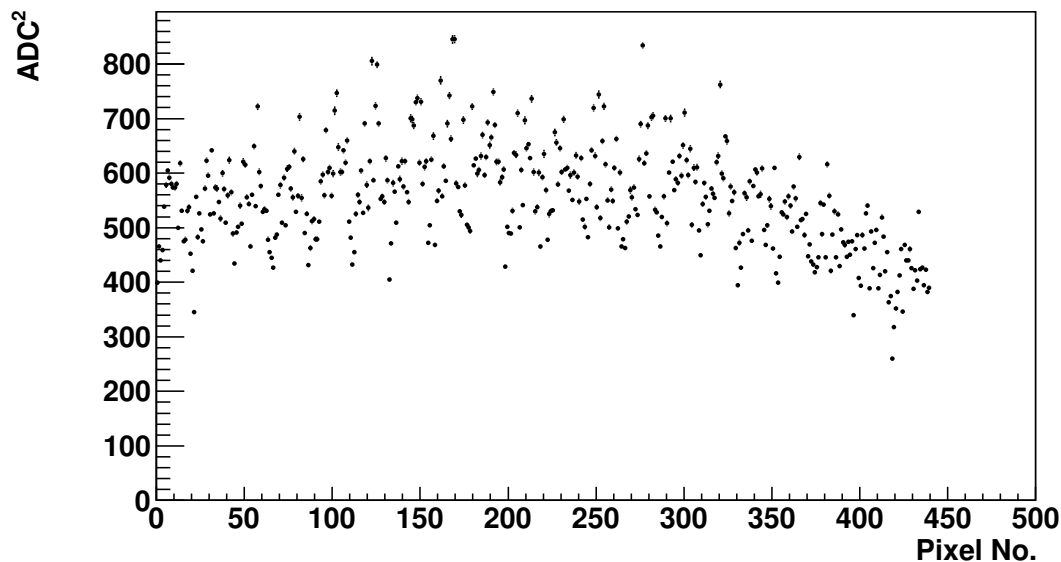


Figure 7.5

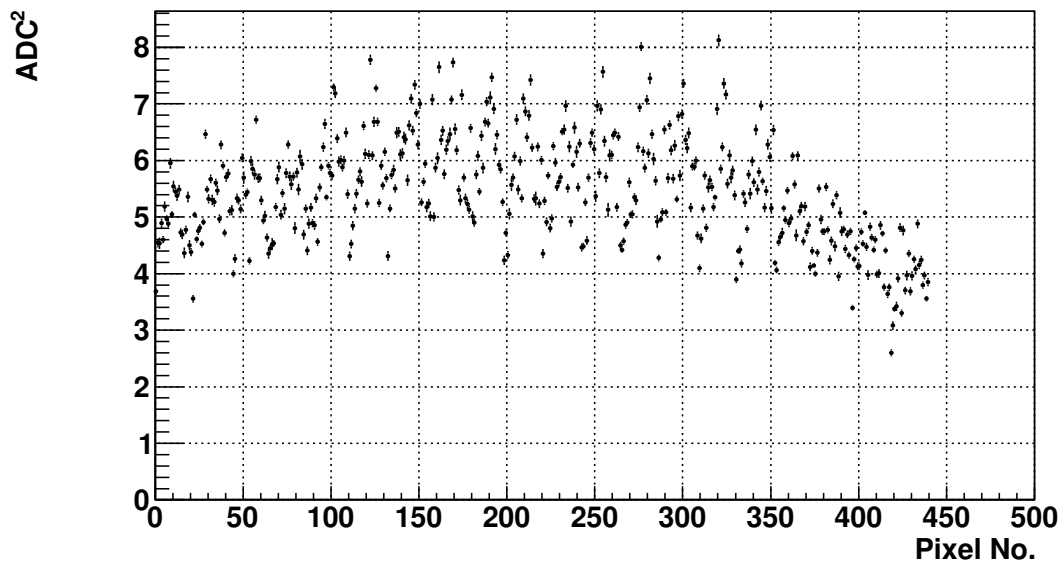


Figure 7.6

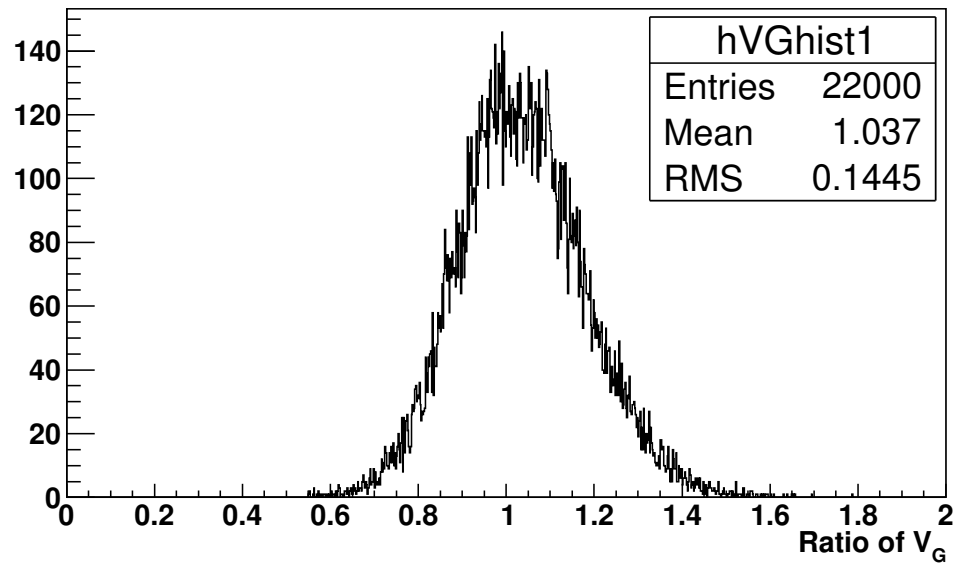


Figure 7.7

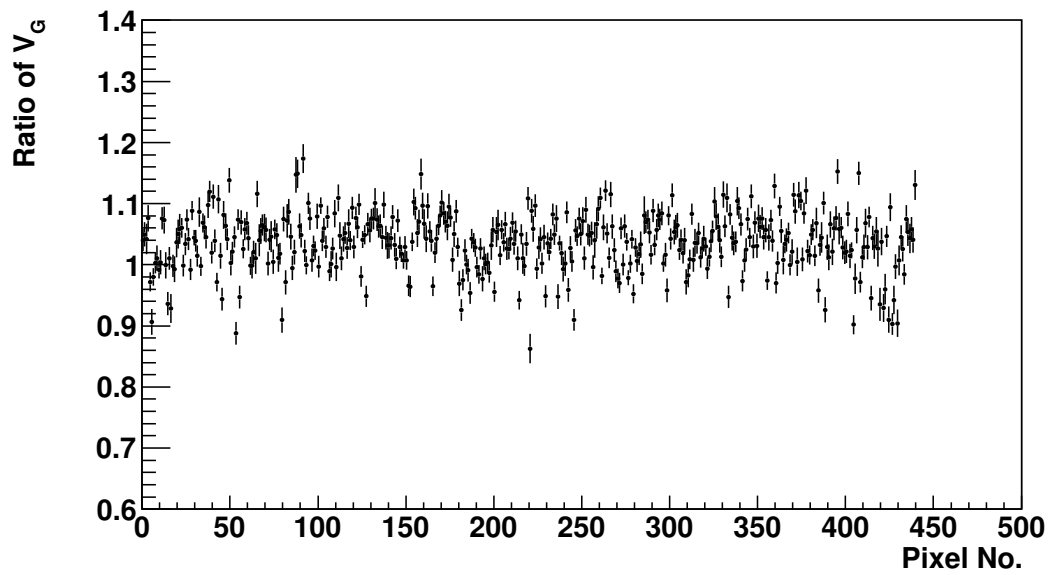


Figure 7.8

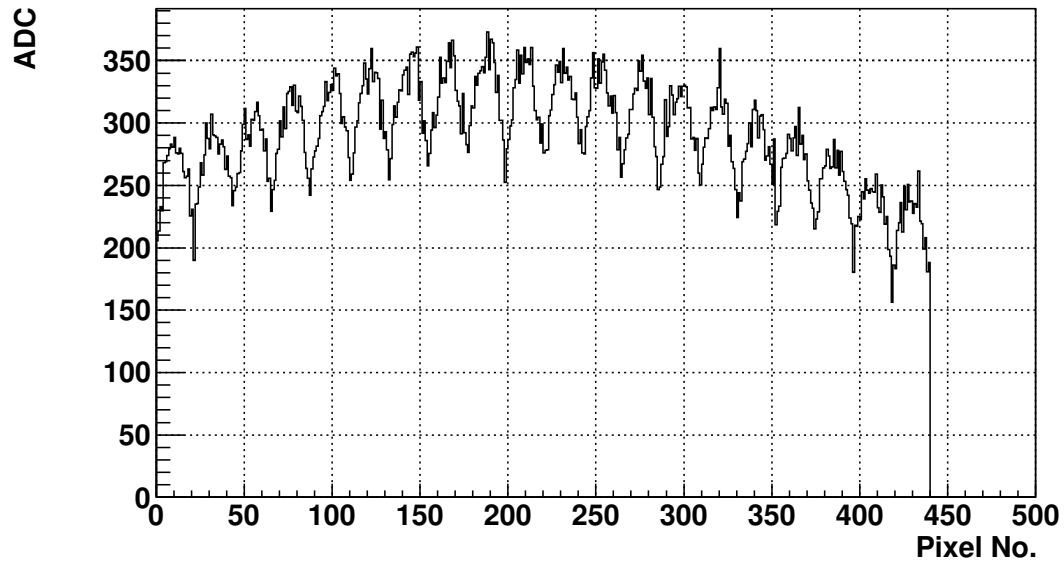


Figure 7.9

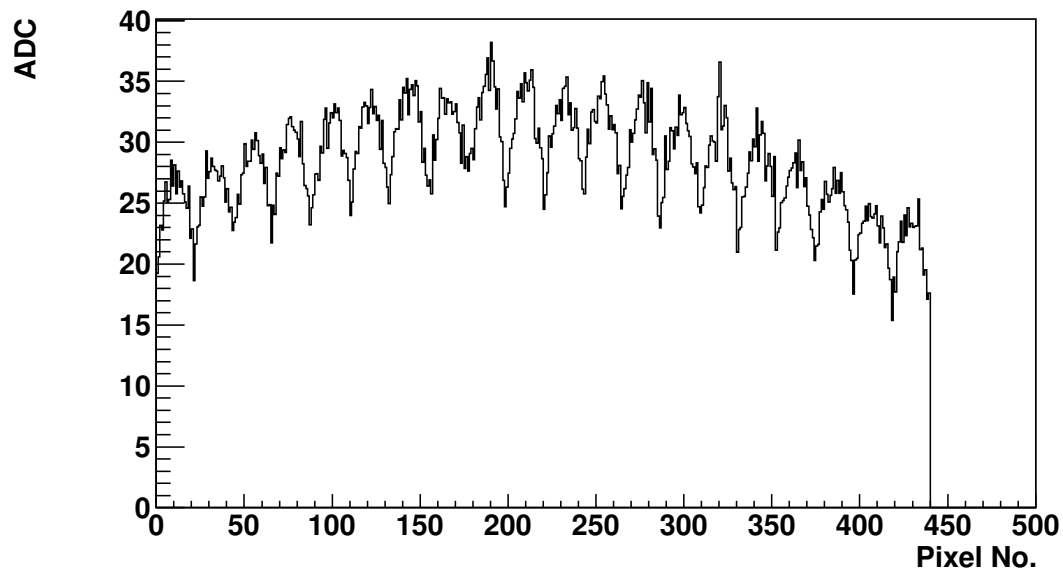


Figure 7.10

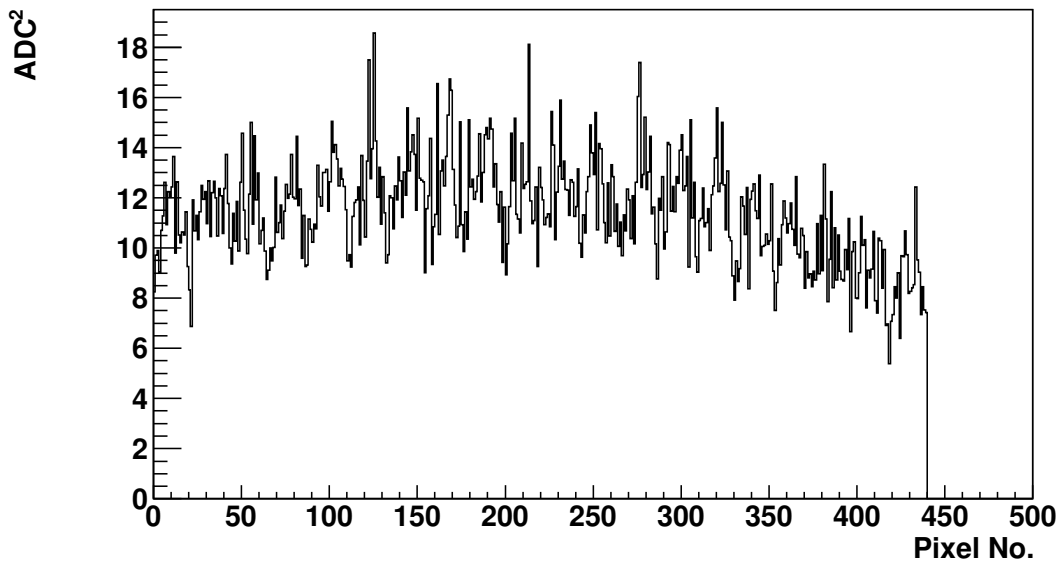


Figure 7.11

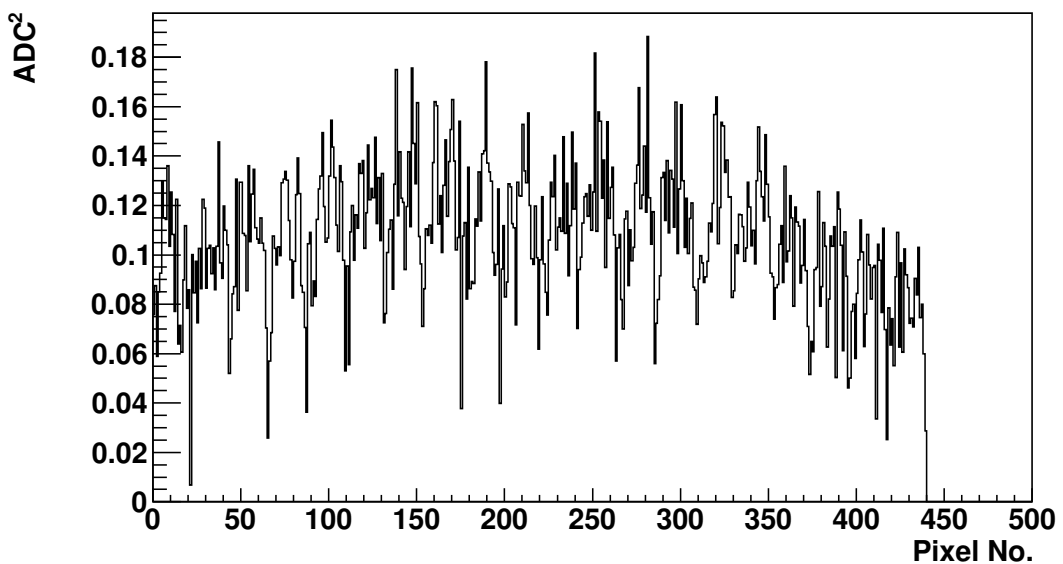


Figure 7.12

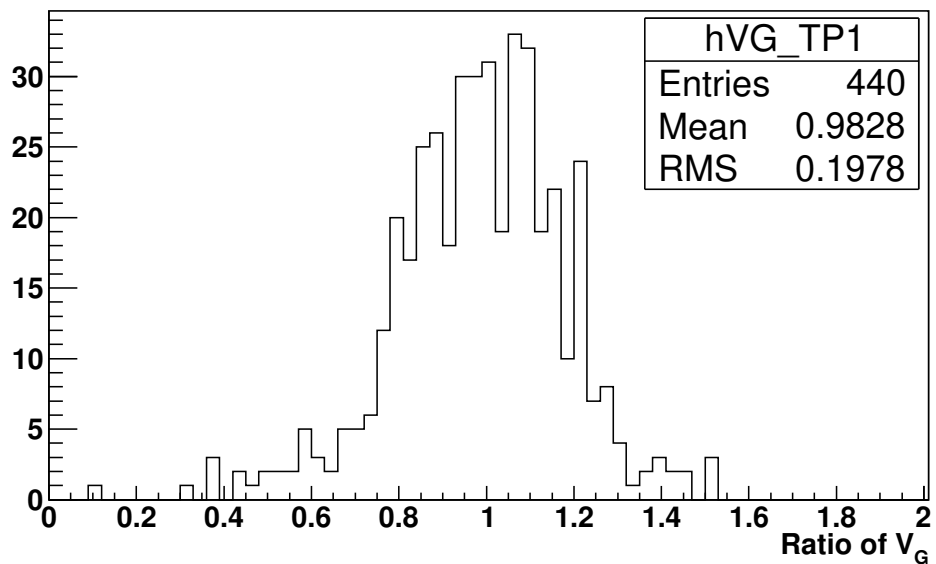


Figure 7.13

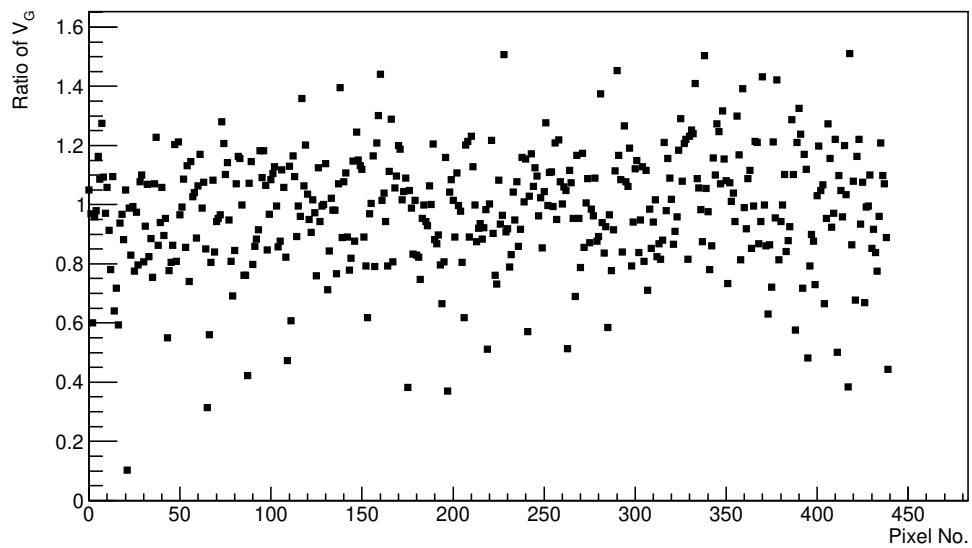


Figure 7.14

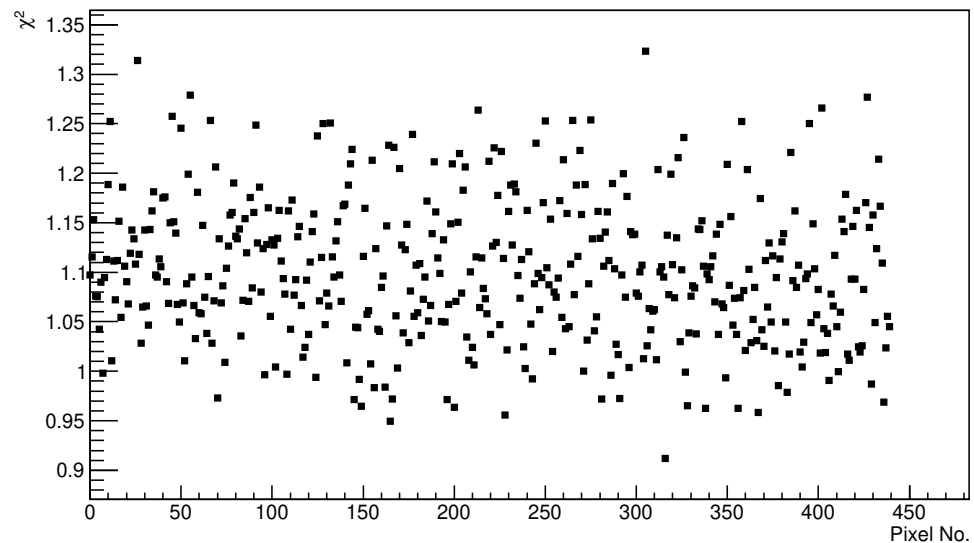


Figure 7.15

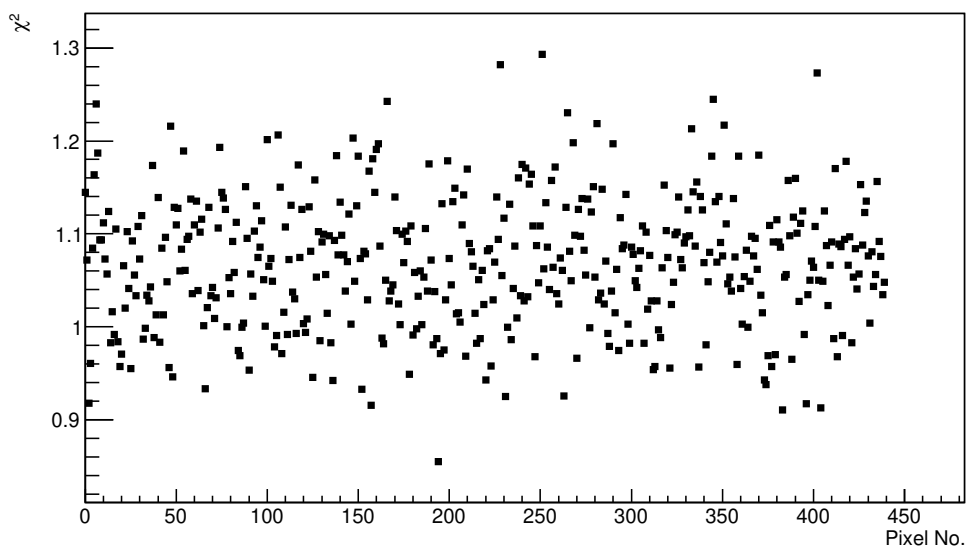


Figure 7.16

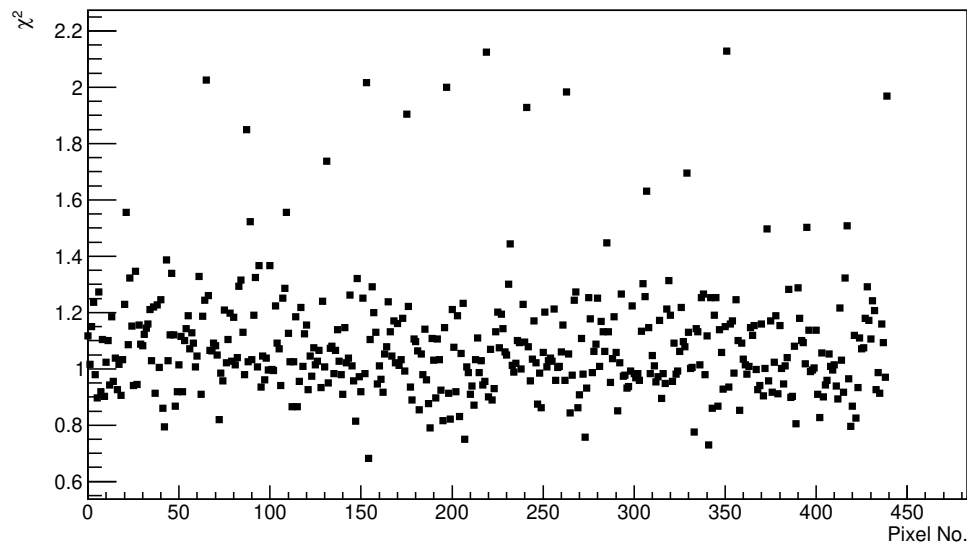


Figure 7.17

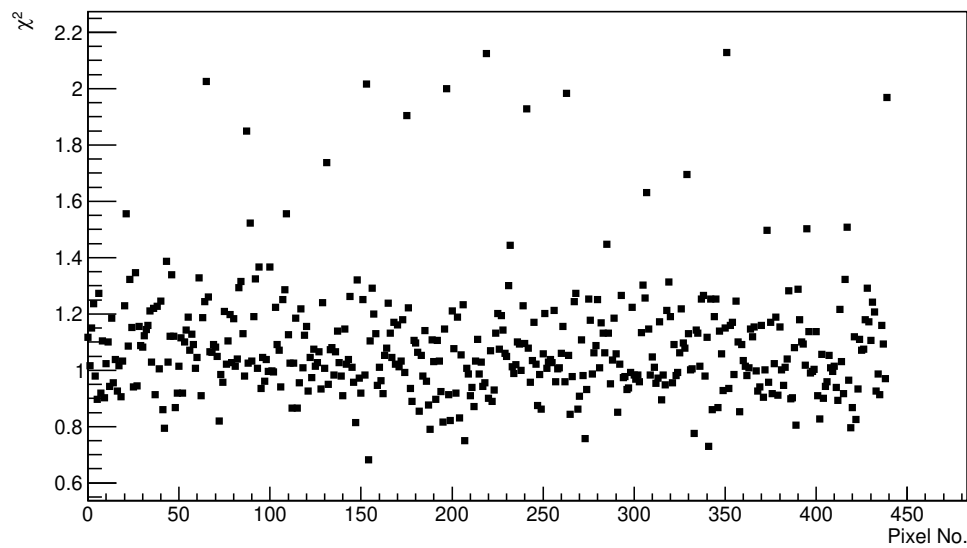


Figure 7.18

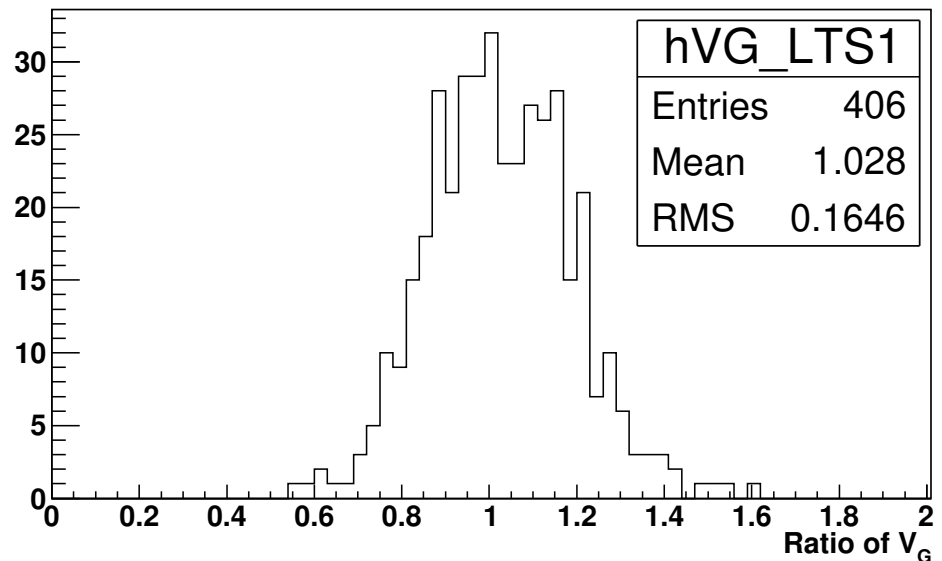


Figure 7.19

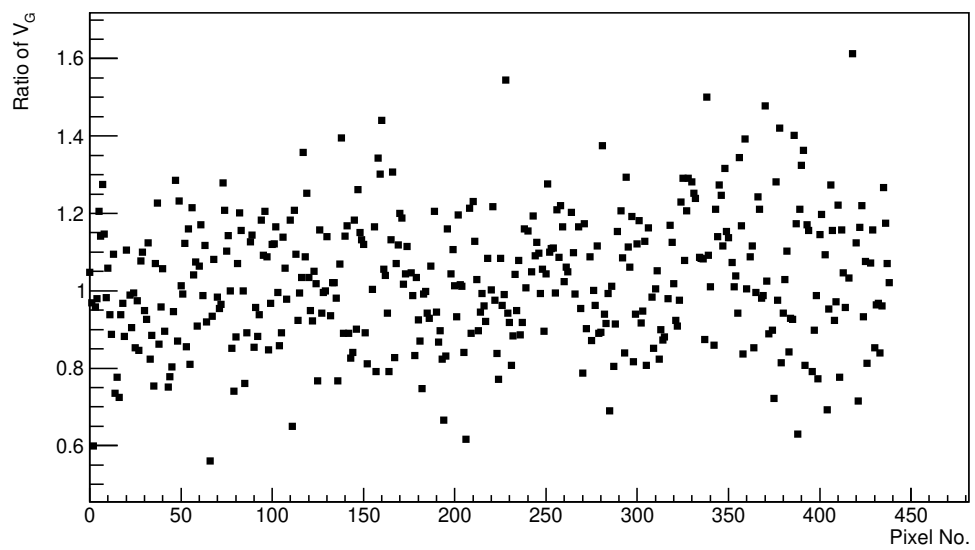


Figure 7.20

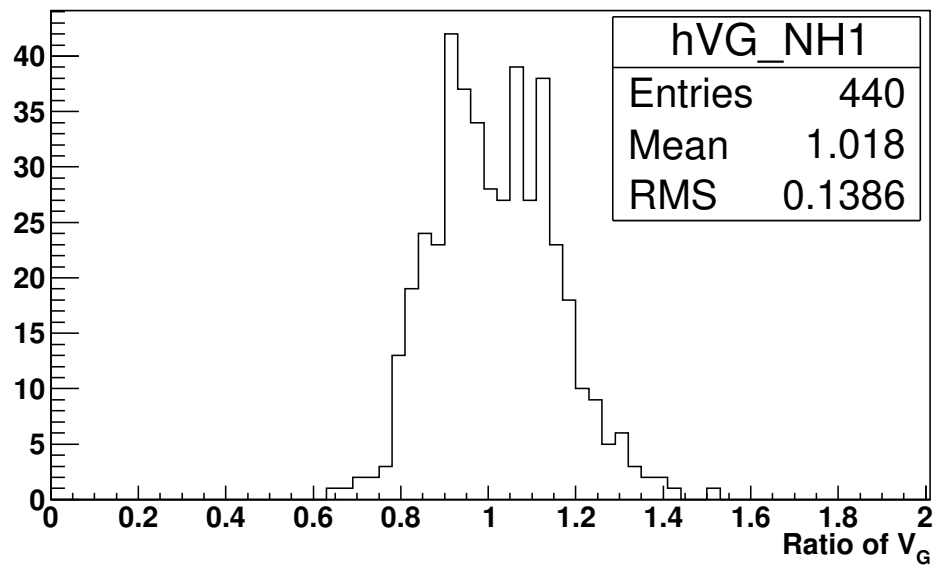


Figure 7.21

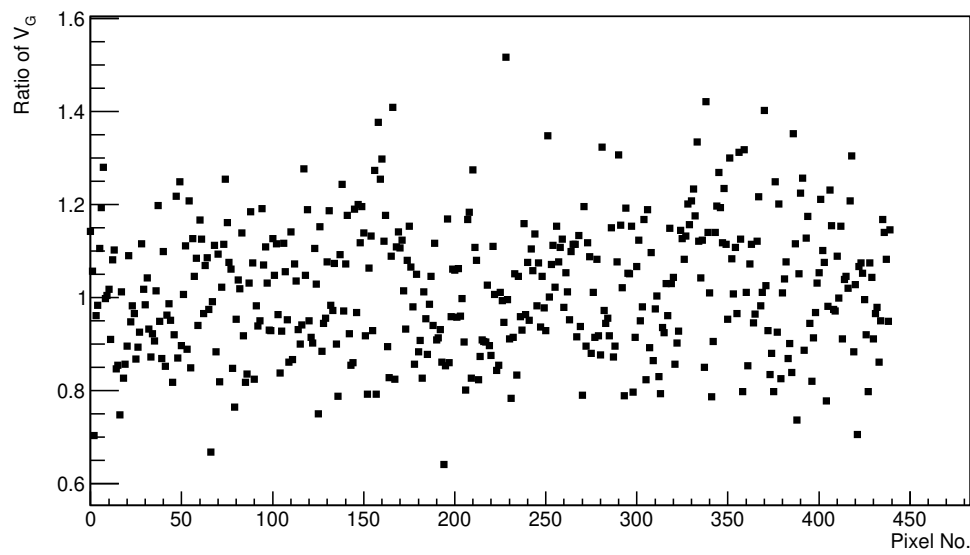


Figure 7.22

Chapter 8

Laboratory Simulation of FD shift

Laboratory Simulation of FD shift under differing NSB levels.

- Measurements for both 900V and 600V (900V used as baseline)
- Different length shifts
- Changing NSB
- measuring how the relevant Gain changes throughout a run

Chapter 9

Evaluation of Cloud Camera Cuts

First look into the effectiveness of the Cloud Camera cuts on PAO Golen Hybrid data.

- Are we being too conservative?
- Effects on Xmax, Zenith and Rp distributions

Chapter 10

Conclusion

10.1 Future Work

Bibliography

- [1] W. Heitler, *The quantum theory of radiation*. Oxford: (Clarendon Press, Ed. 3, Oxford), 1954.